CHALMERS
UNIVERSITY OF TECHNOLOGY

Model-assisted hydronic balancing in residential heating systems using operational sensor data

Downloaded from: https://research.chalmers.se, 2026-11-18 05:37 UTC

Citation for the original published paper (version of record):
[Person 38e92f77-084f-41c0-beee-e1abd1483b61 not found], [Person 9383ad41-b6f6-4bb7-9eeb-5ec2ee1e7fe1 not found], [Person 408ce583-c7eb-4fd5-9a48-a6bff45527e3 not found] et al (2025). Model-assisted hydronic balancing in residential heating systems using operational sensor data. Energy and Buildings, 348. http://dx.doi.org/10.1016/j.enbuild.2025.116464

N.B. When citing this work, cite the original published paper.

research.chalmers.se offers the possibility of retrieving research publications produced at Chalmers University of Technology. It covers all kind of research output: articles, dissertations, conference papers, reports etc. since 2004. research.chalmers.se is administrated and maintained by Chalmers Library

(article starts on next page)

Energy & Buildings 348 (2025) 116464

Contents lists available at ScienceDirect

Energy & Buildings

journal homepage: www.elsevier.com/locate/enbuild

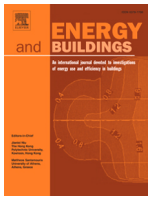

Model-assisted hydronic balancing in residential heating systems using operational sensor data

Henrik Håkansson [a,b,*], Magnus Önnheim [a], Jonas Sjöberg [b], Mats Jirstrand [a,b]

[a] Fraunhofer-Chalmers Centre, Gothenburg, SE-412 88, Sweden
[b] Department of Electrical Engineering, Chalmers University of Technology, Gothenburg, SE-412 96, Sweden

ARTICLE INFO

Keywords:
Hydronic heating
Hydronic balancing
Dynamical modeling
Thermal comfort
Optimization

ABSTRACT

Radiators with improperly calibrated flow rates are common in modern hydronic heating systems, often resulting in undesirable temperature variations across thermal zones. Flow rates are typically regulated by manually adjustable balancing valves installed at various points throughout the hydronic system. Traditionally, these valves are configured using calculations based on data from construction plans. However, these valve configuration often give a zone temperature variance, which can be attributed to commonly occurring discrepancies between the construction plan and the actual building. Consequently, manual rebalancing – an iterative and time-consuming process based on practical heuristics – is often required.

This work addresses these challenges through a model-based approach informed by operational sensor data. Through modeling of the pipe network hydraulics and thermal dynamics of each zone, an expression is derived to evaluate the performance of the radiators' flow rates. Model coefficients are obtained from both the construction plan and through system identification using operational sensor data. This enables evaluation of current system performance and the computation of valve reconfigurations that optimize it. To demonstrate the applicability of the method, a retrospective case study of a rebalancing operation in a Swedish heating system is presented. The analysis indicates that the rebalancing improved the balancing conditions, in line with observed reductions in zone temperature variance. Although the method was not applied during the original rebalancing, the results also suggest that using it could have led to even greater performance improvements.

1. Introduction

Space heating accounts for 30 % of the energy consumed in the EU [1], and improving the efficiency of those systems has been pointed out as an important development area to eventually reach the goal of a carbon-neutral energy system [2]. Many heating systems can be described as various types of hydronic radiator systems [3], which may be used with different kinds of central heat sources such as heat pumps [4], district heating [5], or gas condensing boilers. Reportedly, hydronic radiator systems are often configured to give an unnecessarily high power output, resulting in indoor temperatures well above the levels recommended by the authorities [6]. Hence, there should be a potential to save energy consumption by reducing this overheating by decreasing the margin to the lower comfort limit. What often prevents this from being done is variations in the indoor temperature, both in time and between different thermal zones, that can be attributed to insufficient heat demand control [7]. Due to these variations, an average indoor temperature reduction in a large heating system, e.g., a multi-family dwelling, would typically result in an uncomfortable indoor climate in a subset of the thermal zones. Therefore, it is desirable to avoid these variations by improving the heat demand control mechanisms.

In hydronic radiator systems, hot water is pumped from a central heat source to radiators located inside the thermal zones, where the water is cooled by heat transfer to the inside air and eventually recirculated to the central heat source [8]. The delivered heat is a function of water temperature and flow rate, which is utilized in the common control mechanisms. The probably most basic setup is to only have automatic control centrally, with the supply water temperature set by a feedforward controller from the outdoor temperature, known as weather-compensated control. To allocate the heating power appropriately between the thermal zones, there are *balancing valves* which are manually adjusted to obtain appropriate flow rates in the radiators. With no automatic feedback from the indoor temperature, such simple setups are often poorly tuned, such that overheating is common [9]. By also introducing thermostatic radiator valves (TRVs), automatic control is also enabled locally since TRVs adjust the flow rate with feedback from the

* Corresponding author.
E-mail address: henhak@chalmers.se (H. Håkansson).

https://doi.org/10.1016/j.enbuild.2025.116464
Received 19 June 2025; Received in revised form 29 August 2025; Accepted 15 September 2025
Available online 18 September 2025
0378-7788/© 2025 The Author(s). Published by Elsevier B.V. This is an open access article under the CC BY license (http://creativecommons.org/licenses/by/4.0/).

indoor temperature in the thermal zone [10]. The commonly used mechanical TRVs can, however, only perform well within a limited flow range [11], meaning that the control performance of the TRVs is degraded if balancing valves are inappropriately set [12–14]. Therefore, properly done hydronic balancing, i.e., by configuring balancing valves, is crucial for achieving successful heat demand control in all thermal zones regardless of whether TRVs are installed or not [10,15,16].

Poorly balanced hydronic heating systems have been recognized as an obstacle in the current building stock to achieve more energy-efficient control [17]. The typical balancing strategy starts by calculating a flow rate, or a configuration, for each balancing valve, based on information from the construction plan [14,18]. After disabling TRVs, if such are installed, a technician initially adjusts the balancing valves according to the calculation [19], but due to discrepancies between the construction plan and the actual system, this procedure may often not provide a satisfactory heat allocation to at least some of the thermal zones. Consequently, there is a significant temperature variance even after the initial configuration, which a technician has to mitigate with a time-consuming trial-and-error approach to redistribute the flow rate by reconfiguring the valves. Also, since system properties may change over time, e.g., changes in thermal characteristics due to replacement of components, hydronic balancing needs to be performed regularly.

Finding alternatives and improvements that facilitate hydronic balancing, and ultimately automate the manual work [20], is thus necessary to optimize the efficiency of the present hydronic systems. There have been several developments of flow control equipment, e.g., pressure-independent balancing valves [10,18,21] and motorized TRVs [22], that have showed improvements of the balancing conditions. Yet, such setups are still rare in Swedish dwellings due to the extra investment costs [23]. On the other hand, many housing companies have recently installed temperature sensors inside apartments to enable feedback control for the central heating power [7]. Although such efforts of improving the central control have led to significant energy savings, the potential is limited since only the accumulated heating power of all apartments is affected, and thereby only the average indoor temperature. With insufficient local conditions, there will always be temperature variations in individual apartments, and some degree of overheating will be necessary to avoid discomfort [24]. Sarran et al. [25] developed a data-based approach for diagnosing the balancing conditions in a modern building equipped with electronic TRVs and heat meters. While most apartment buildings in Sweden have a simpler setup, consisting of only an indoor temperature sensor in each apartment, it is still possible to retrieve information about the heat allocation of the radiator system as obtained through balancing.

In recent years, the interest in data-driven modeling for thermal dynamics in heating systems in general has increased [26]. The main reason behind this movement is the simultaneously increased interest in model predictive control (MPC) for central control [27]. Within this field, gray-box approaches have been regarded as attractive since they often offer both interpretability and decent model quality to relatively little effort [28]. A hydronic heating system may be particularly challenging to model due to the non-linearities of the hydronic radiators, but studied model complexity includes both rather detailed models of those nonlinearities [29,30] and linear approximations [31]. For the case of MPC, there are results suggesting that simple models may perform as well as more complex [32]. It should, however, be pointed out that none of the aforementioned works considers modeling for assisting hydronic balancing, which arguably introduces other requirements than what is needed for a model to be used in a feedback controller.

This work presents a modeling approach for assisting the rebalancing work using both construction plan data and operational time-series data collected from sensors in all thermal zones. This sensor setup reflects recent installations by housing companies aimed at enabling centralized feedback control. Unlike conventional methods, which are based solely on the construction plan and do not assess the actual thermal state of the system, the proposed approach uses operational data to evaluate the current hydronic balancing status. Based on this evaluation, potential valve reconfigurations can also be calculated to improve balancing conditions.

1.1. Outline

The remainder of this paper is structured as follows: Section 2 outlines the aims of this work and specifies the data and system information required to apply the proposed methods. Section 3 introduces modeling for evaluating the performance of flow rates and valve configurations. Section 4 builds on the modeling in Section 3 to derive tools for assisting rebalancing using the data listed in Section 2. Section 5 demonstrates the application of these tools through a retrospective analysis of a rebalancing operation carried out in a Swedish heating system. Lastly, Section 6 discusses the results from the case study and suggests refinements to the approach.

2. Problem formulation

We consider a hydronic heating system with a central heat source and a pump that serves radiators in different thermal zones. The pipe system is a two-pipe system, i.e., each radiator is connected to a supply pipe and a return pipe, and the pump operates with a known constant differential pressure. The supply temperature of the heat source can be controlled in real time, and there are balancing valves that can be manually configured to affect the distribution of flow rates to the different radiators. We have time-series data consisting of the supply and return temperature of the central heat source, the outdoor temperature, and the air temperature from each thermal zone. With access to the construction plan, we also have information about the full pipe network, accompanied by lengths, diameters, and materials. We have a protocol with the valves' current configurations and flow rates, and we know the valve types and their corresponding specification.

The overall performance objective addressed in this work is to track the same reference temperature in each thermal zone, meaning that we aim to eliminate any temperature variance in time or across thermal zones. Given this objective, the problem we focus on in this work is to use the earlier-mentioned data to configure the manual balancing valves to facilitate successful automatic control.

3. Modeling of balancing performance

For a hydronic system with radiators $r = 1, \dots, R$, the heating power delivered at time t by radiator r is denoted by $\Phi_r(t \mid u_{\le t}, q_{\mathrm{rad},r}(\boldsymbol{k}_{\mathrm{val}}))$, which is given by the past and current supply temperature $u_{\le t} = \{u(s) \mid s \le t\}$ and the static radiator flow rate $q_{\mathrm{rad},r}$, which in turn is a function of the static valve configurations $\boldsymbol{k}_{\mathrm{val}} \in \mathbb{R}^V$ of all valves $v = 1, \dots, V$. The radiators in a thermal zone $z = 1, \dots, Z$ have indices $r = P_z, \dots, R_z$. The temperature in zone z at time t, $y_z(t)$, depends on the past and current heating power $\Phi_{r,\le t}(u_{\le t}, q_{\mathrm{rad},r}(\boldsymbol{k}_{\mathrm{val}})) = \{\Phi_r(s) \mid s \le t\}$ of the zone's radiators $r = P_z, \dots, R_z$, but also past and current disturbances $W_{z,\le t} = \{W(s) \mid s \le t\}$ mainly from the weather conditions. The objective when controlling the supply temperature u and configuring the valves with $\boldsymbol{k}_{\mathrm{val}}$ is to generate radiator heating powers $\boldsymbol{\Phi}_{\le t}\big(u_{\le t}, \boldsymbol{q}_{\mathrm{rad}}\big(\boldsymbol{k}_{\mathrm{val}}\big)\big) = \big[\Phi_{1,\le t}, \dots, \Phi_{R,\le t}\big]^\top$ such that the zone temperatures $\boldsymbol{y}(t) = \big[y_1(t), \dots, y_Z(t)\big]^\top$ are close to the reference temperature y_{ref} at each time t. That is, the norm of the vector of errors in each zone

$$\boldsymbol{e}\big(t \mid \boldsymbol{\Phi}_{\le t}, \boldsymbol{W}_{\le t}\big) = \mathbb{1}\, y_{\mathrm{ref}} - \boldsymbol{y}(t \mid \boldsymbol{\Phi}_{\le t}, \boldsymbol{W}_{\le t}). \tag{1}$$

should be desirably small at each time t. The balancing performance for the valve configurations $\boldsymbol{k}_{\mathrm{val}}$ is formulated as the asymptotic integrated squared error norm produced by the valve configurations $\boldsymbol{k}_{\mathrm{val}}$ and an

optimally controlled supply temperature $u_{\leq T}$

$$J(\boldsymbol{k}_{\text{val}}) = \lim_{T\to\infty} \min_{u_{\leq T}} \frac{1}{T} \int_0^T \left\| \boldsymbol{e}\left(t \mid \boldsymbol{\Phi}_{\leq t}\left(u_{\leq t}, \boldsymbol{q}_{\text{rad}}(\boldsymbol{k}_{\text{val}})\right), \boldsymbol{W}_{\leq t}\right)\right\|_2^2 dt. \tag{2}$$

In the remainder of this section, an upper bound of the performance $J(\boldsymbol{k}_{\text{val}})$ is derived by modeling the thermal and hydraulic characteristics of the hydronic system. In Section 3.1, the connection between valve configurations $\boldsymbol{k}_{\text{val}}$ and the radiator flow rates $\boldsymbol{q}_{\text{rad}}$ is modeled via non-linear equations and inequalities based on the pipe system hydraulics. In Section 3.2, the dynamics of the error in Eq. (1), $\dot{\boldsymbol{e}}$, is modeled by considering the thermal balance in each zone. Finally, in Section 3.3, the upper bound for the balancing performance $J(\boldsymbol{k}_{\text{val}})$ is derived by using the hydraulic model from Section 3.1 and the error dynamics model from Section 3.2.

3.1. Modeling radiator flow rates

The relation between valve configurations $\boldsymbol{k}_{\text{val}}$ and radiator flow rates $\boldsymbol{q}_{\text{rad}}$ is modeled from the hydraulics of the whole pipe system. The hydraulic model is formulated using a directed graph structure with edges $a = 1, \dots, R+V+S$, corresponding to the R radiators, V valves, and S pipe sections. The edges are ordered by the component types as follows:

$$a = \underbrace{1, \dots, R}_{R \text{ radiators}}, \underbrace{R+1, \dots, R+V}_{V \text{ valves}}, \underbrace{R+V+1, \dots, R+V+S}_{S \text{ pipe sections}}. \tag{3}$$

The graph's vertices are indexed $b = 1, \dots, B$, where vertex $b = 1$ is located at the outlet of the pump and vertex $b = B$ is located at the pump's inlet. Thus, all flow paths of the pipe network start in $b = 1$ and end in $b = B$. $\delta^+(b)$ and $\delta^-(b)$ denote the sets of outgoing and incoming edges at a vertex b, and $\sigma^h(a)$ and $\sigma^t(a)$ for the head and tail vertices of an edge a. The graph structure is schematically visualized in Fig. 1.

Each edge a has a flow rate q_a and hydraulic resistance k_a, and each vertex b has a pressure p_b relative to the lowest pressure in the system at $b = B$. The basic hydraulics in the pipe network is described with the following set of equations and inequalities

$$\begin{cases} 0 \leq q_a & & \text{(4a)} \\ \sum_{a\in\delta^+(b)} q_a = \sum_{a\in\delta^-(b)} q_a & b = 2, \dots, B-1 & \text{(4b)} \\ p_{\sigma^h(a)} - p_{\sigma^t(a)} = k_a\, q_a^2 & a = 1, \dots, R+V+S & \text{(4c)} \\ p_1 = \Delta p_{\text{pump}} & & \text{(4d)} \\ p_B = 0, & & \text{(4e)} \end{cases}$$

where Eq. (4b) models conservation of mass at a vertex b, whereas Eq. (4c) models the pressure drop across an edge a by the quadratic flow rate q_a^2 and the hydraulic resistance k_a [13], Eq. (4d) and (4e) models the total pressure drop for all flow paths to equal the pump's differential pressure Δp_{pump}, and Eq. (4a) ensures non-negative flow rates q_e.

The modeling of the hydraulic resistance k_a depends on the type of edge a. For a valve v, corresponding to the edge $a = R + v$, the resistance $k_{R+v} = k_{\text{val},v}$ is the adjustable configuration which can be set to any value between its lower clamp capacity $L_{\text{val},v}$ and upper clamp capacity $U_{\text{val},v}$. For a radiator r, corresponding to the edge $a = r$, the resistance $k_r = k_{\text{rad,r}}$ is assumed to be a fixed known resistance $\tilde{k}_{\text{rad},r}$. For a pipe s, corresponding to the edge $a = R+V+s$, the resistance $k_{R+V+s} = k_{\text{pip},s}$ is calculated using standard models given by its properties concerning its diameter d_s, length l_s, pipe roughness ε_s, and friction factor f_s. The water density is denoted ρ, and the dynamic viscosity of water is denoted μ. Altogether, the resistances of all edges are modeled by

$$\begin{cases} L_{\text{val},v} \leq k_{\text{val},v} \leq U_{\text{val,v}} & v = 1, \dots, V \text{ (5a)} \\ k_{\text{rad},r} = \tilde{k}_{\text{rad},r}, & r = 1, \dots R \text{ (5b)} \\ k_{\text{pip},s} = \frac{8\rho l_s f_s}{\pi^2 d_s^5} & s = 1, \dots, S \text{ (5c)} \\ \frac{1}{\sqrt{f_s}} = -2\log_{10}\left(\frac{2.51\,\pi\, d_s\, \mu}{4\,\rho\, q_{\text{pip},s}\sqrt{f_s}} + \frac{\varepsilon_s}{3.72\, d_s}\right) & s = 1, \dots, S, \text{ (5d)} \end{cases}$$

where Eq. (5a) sets the bounds on the valve configuration, Eq. (5b) models the constant radiator resistance, Eq. (5c) models the pipe resistance using the Darcy-Weisbach equation [8], and Eq. (5d) is the Colebrook equation [8] which implicitly gives the pipe friction factor f_s.

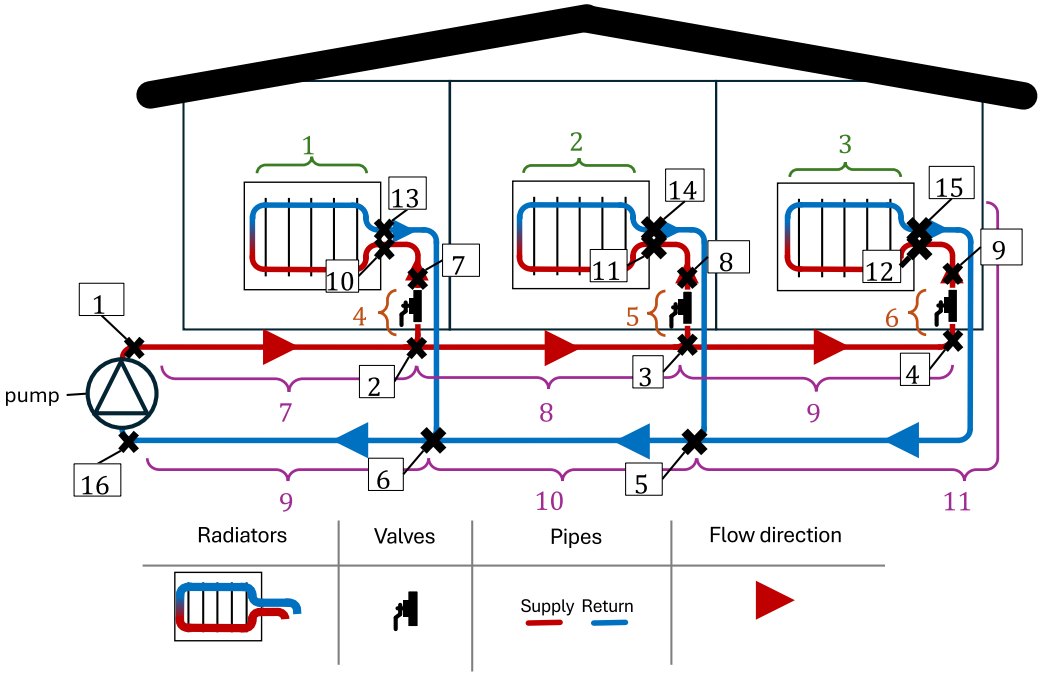

Fig. 1. Schematic of the directed graph used for hydraulic modeling of the example heating system visualized in Fig. 2 where $R = 3$, $V = 3$, $S = 11$, and $B = 16$. Crosses denote the vertices $b = 1, \dots, 16$ with the corresponding indices in the boxes. Edges are marked by brackets and colored by the edge type: green radiator edges $a = 1, 2, 3$, orange valve edges $a = 4, 5, 6$, and purple pipe section edges $a = 7, \dots, 11$. Due to limited space, pipe section edges $a = 12, \dots, 17$ are not labeled. The heat source, which is located close to the pump, is omitted in this view. (For interpretation of the references to colour in this figure legend, the reader is referred to the web version of this article.)

Given values of the pump's differential pressure Δp_{pump}, constant radiator resistances $\tilde{\boldsymbol{k}}_{\text{rad}}$, lower valve configurations $L_{\text{val,v}}$, upper valves configurations $U_{\text{val,v}}$, pipe diameters $\boldsymbol{d}$, pipe lengths $\boldsymbol{l}$, pipe roughnesses $\boldsymbol{\varepsilon}$, the set of equations and inequalities in Eqs. (4) and (5) gives a feasible set of edge flow rates $\boldsymbol{q} = \left[\boldsymbol{q}_{\text{rad}}^\top, \boldsymbol{q}_{\text{val}}^\top, \boldsymbol{q}_{\text{pip}}^\top\right]^\top$, edge resistances $\boldsymbol{k} = \left[\boldsymbol{k}_{\text{rad}}^\top, \boldsymbol{k}_{\text{val}}^\top, \boldsymbol{k}_{\text{pip}}^\top\right]^\top$, vertex pressures $\boldsymbol{p}$, and pipe friction factors $\boldsymbol{f}$. By separating the inequalities and equations in Eqs. (4) and (5), the feasible set of $\boldsymbol{q}, \boldsymbol{k}, \boldsymbol{p}, \boldsymbol{f}$ is denoted as

$$\begin{cases} \text{Eqs. (4a) and (5a)} \\ \text{Eqs. (4b) to (4e) and (5b) to (5d)} \end{cases} \iff \begin{cases} \boldsymbol{0} \le \boldsymbol{g}(\boldsymbol{q}, \boldsymbol{k} \mid \boldsymbol{L}_{\text{val}}, \boldsymbol{U}_{\text{val}}) \\ \boldsymbol{0} = \boldsymbol{h}(\boldsymbol{q}, \boldsymbol{k}, \boldsymbol{p}, \boldsymbol{f} \mid \Delta p_{\text{pump}}, \tilde{\boldsymbol{k}}_{\text{rad}}, \boldsymbol{d}, \boldsymbol{l}, \boldsymbol{\varepsilon}) \end{cases} \tag{6}$$

Since the radiator flow rates $\boldsymbol{q}_{\text{rad}}$ is a subset of all edge flow rates $\boldsymbol{q}$, and the valve configurations $\boldsymbol{k}_{\text{val}}$ is a subset of all edge resistances, the relation $\boldsymbol{q}_{\text{rad}}(\boldsymbol{k}_{\text{val}})$, appearing in Eq. (2), is implicitly modeled with Eq. (6).

3.2. Modeling error dynamics

The rate of change of the air temperature $\dot{y}_z$ in zone z is modeled as

$$\dot{y}_z(t) = \theta_z \left(w(t) - y_z(t)\right) + C_z \sum_{r=P_z}^{R_z} \Phi_r(t) \tag{7}$$

where θ_z is a lumped parameter for the thermal leakage through the building envelope in zone z, $w(t)$ is the outdoor temperature at time t, C_z is a zone-specific parameter in K/W·s for converting heating power Φ_r from the zone's radiators $r = P_z, \dots, R_z$ to a temperature. By linearizing a radiator's heat output Φ_r with respect to supply temperature u and zone temperature y_z, and by approximating all radiators in a zone as one single radiator, which is described in more detail in Appendix A, the heating terms in Eq. (7) are approximated as

$$C_z \sum_{r=P_z}^{R_z} \Phi_r(t) \approx \nu_z\left(q_{\text{zon},z}\right)\,(u(t) - y_z(t)), \tag{8}$$

where

$$q_{\text{zon},z} = \sum_{r=P_z}^{R_z} q_{\text{rad},r} \tag{9}$$

is the summed flow rate of the radiators, and ν_z is a *heat supply coefficient* given by

$$\nu_z(q_{\text{zon},z}) = C_z\, c_p\, q_{\text{zon},z} \left(1 - \exp\left(-\frac{(R_z - P_z + 1)\, L_z\, m_z}{c_p\, q_{\text{zon},z}}\right)\right), \tag{10}$$

where c_p is the specific heat capacity of water, L_z is the length of a radiator, and m_z is a radiator-specific heat transfer coefficient. Due to the linearized heat transfer, the coefficient m_z is valid for an operating range of supply temperature u and zone temperature y_z. The approximation of treating all the zone's radiators as one is reasonable when the flow rates of the zone's radiators $q_{\text{rad},P_z}, \dots, q_{\text{rad},R_z}$ are close to the zonal average flow rate $q_{\text{zon},z}/(R_z - P_z + 1)$, which is explained further in Appendix A. From Eq. (7), and with the radiator approximation in Eq. (8), the model for the thermal dynamics of zones is

$$\begin{aligned} \dot{\boldsymbol{y}}(t) &= \operatorname{diag}(\boldsymbol{\theta})\,(\mathbb{1}\, w(t) - \boldsymbol{y}(t)) + \operatorname{diag}(\boldsymbol{\nu}(\boldsymbol{q}_{\text{rad}}))\,(\mathbb{1}\, u(t) - \boldsymbol{y}(t)) \\ &= -\operatorname{diag}(\boldsymbol{\theta} + \boldsymbol{\nu}(\boldsymbol{q}_{\text{rad}}))\,\boldsymbol{y}(t) + \boldsymbol{\theta}\, w(t) + \boldsymbol{\nu}(\boldsymbol{q}_{\text{rad}})\, u(t), \end{aligned} \tag{11}$$

where $\boldsymbol{y}(t) = [y_1(t), \dots, y_Z(t)]^\top$, $\boldsymbol{\theta} = \left[\theta_1, \dots, \theta_Z\right]^\top$ and $\boldsymbol{\nu}(\boldsymbol{q}_{\text{rad}}) = \left[\nu_1(q_{\text{zon},1}), \dots, \nu_Z(q_{\text{zon},Z})\right]^\top$. A schematic visualization of the thermal model Eq. (11) can be seen in Fig. 2.

With the error $\boldsymbol{e}(t)$ defined in Eq. (1), the error dynamics given the thermal model in Eq. (11) is

$$\begin{aligned} \dot{\boldsymbol{e}}(t) &= \frac{d}{dt}(\mathbb{1}\, y_{\text{ref}} - \boldsymbol{y}(t)) \\ &= -\,\dot{\boldsymbol{y}}(t) \\ &= \operatorname{diag}(\boldsymbol{\theta} + \boldsymbol{\nu}(\boldsymbol{q}_{\text{rad}}))\,\boldsymbol{y}(t) - \boldsymbol{\theta}\, w(t) - \boldsymbol{\nu}(\boldsymbol{q}_{\text{rad}})\, u(t) \\ &= \operatorname{diag}(\boldsymbol{\theta} + \boldsymbol{\nu}(\boldsymbol{q}_{\text{rad}}))\,\boldsymbol{y}(t) - \boldsymbol{\theta}\, w(t) - \boldsymbol{\nu}(\boldsymbol{q}_{\text{rad}})\, u(t) \\ &\quad + (\boldsymbol{\theta} + \boldsymbol{\nu}(\boldsymbol{q}_{\text{rad}}))\,(y_{\text{ref}} - y_{\text{ref}}) \\ &= -\operatorname{diag}(\boldsymbol{\theta} + \boldsymbol{\nu}(\boldsymbol{q}_{\text{rad}}))\,\boldsymbol{e}(t) + \boldsymbol{\theta}\,(y_{\text{ref}} - w(t)) \\ &\quad + \boldsymbol{\nu}(\boldsymbol{q}_{\text{rad}})\,(y_{\text{ref}} - u(t)). \end{aligned} \tag{12}$$

3.3. Upper bound of balancing performance

To create an upper bound for the performance $J(\boldsymbol{k}_{\text{val}})$, the supply temperature $u(t)$ is assumed to be regulated by using feedback of the error $\boldsymbol{e}(t)$ and feed-forward of the outdoor temperature $w(t)$ according to the control law

$$u(t) = y_{\text{ref}} - \boldsymbol{F}_e^\top\, \boldsymbol{e}(t) - F_w\,(y_{\text{ref}} - w(t)), \tag{13}$$

where $\boldsymbol{F}_e \in \mathbb{R}^Z$ is the static feedback gain, $F_w \in \mathbb{R}$ is the static feed-forward gain. With such a regulator, the resulting error dynamics are

$$\begin{aligned} \dot{\boldsymbol{e}}(t) &= \left(-\operatorname{diag}(\boldsymbol{\theta} + \boldsymbol{\nu}(\boldsymbol{q}_{\text{rad}})) + \boldsymbol{\nu}(\boldsymbol{q}_{\text{rad}})\,\boldsymbol{F}_e^\top\right)\boldsymbol{e}(t) \\ &\quad + (\boldsymbol{\theta} + F_w\,\boldsymbol{\nu}(\boldsymbol{q}_{\text{rad}}))\,(y_{\text{ref}} - w(t)). \end{aligned} \tag{14}$$

The error dynamics are inherently exponentially stable, since $\boldsymbol{0} < \boldsymbol{\theta}$ and $\boldsymbol{0} \le \boldsymbol{\nu}(\boldsymbol{q}_{\text{rad}})$. The feedback term $\boldsymbol{\nu}(\boldsymbol{q}_{\text{rad}})$ is used to improve control performance, and if it is sufficiently small, it will not compromise stability. Without loss of generality, assuming a zero-error initial state $\boldsymbol{e}(0) = \boldsymbol{0}$ gives the bound on the squared error norm at time t

$$\|\boldsymbol{e}(t)\|_2^2 \le \left\|\boldsymbol{\theta} + F_w\,\boldsymbol{\nu}(\boldsymbol{q}_{\text{rad}})\right\|_2^2 \mathcal{I}(t), \tag{15}$$

where

$$\mathcal{I}(t) = \int_0^t \gamma\, \exp\left(-\lambda\,(t - \tau)\right) \left\|y_{\text{ref}} - w(t - \tau)\right\|_2^2 d\tau \tag{16}$$

and γ and λ are some finite positive constants. A proof for Eq. (15) can be found in, e.g., Rugh [33]. At any time step t, the upper bound in Eq. (15) is minimized by setting the feed-forward gain F_w as

$$F_w = \arg\min_{F_w} \left\|\boldsymbol{\theta} + F_w \boldsymbol{\nu}(\boldsymbol{q}_{\text{rad}})\right\|_2^2 = -\frac{\boldsymbol{\theta}^\top\, \boldsymbol{\nu}(\boldsymbol{q}_{\text{rad}})}{\left\|\boldsymbol{\nu}(\boldsymbol{q}_{\text{rad}})\right\|_2^2}. \tag{17}$$

With the *performance proxy*

$$\begin{aligned} L(\boldsymbol{q}_{\text{rad}}) &= \min_{F_w} \left\|\boldsymbol{\theta} + F_w \boldsymbol{\nu}(\boldsymbol{q}_{\text{rad}})\right\|_2^2 \\ &= \left\|\boldsymbol{\theta} - \frac{\boldsymbol{\theta}^\top\, \boldsymbol{\nu}(\boldsymbol{q}_{\text{rad}})}{\left\|\boldsymbol{\nu}(\boldsymbol{q}_{\text{rad}})\right\|_2^2}\, \boldsymbol{\nu}(\boldsymbol{q}_{\text{rad}})\right\|_2^2, \end{aligned} \tag{18}$$

where valve configurations $\boldsymbol{k}_{\text{val}}$ and radiator flow rates $\boldsymbol{q}_{\text{rad}}$, subsets of all edge resistances $\boldsymbol{k}$ and edge flow rates $\boldsymbol{q}$, forms a feasible solution together with pressures $\boldsymbol{p}$ and pipe friction factors $\boldsymbol{f}$ of the hydraulic model in Eq. (6),

$$\begin{aligned} &\boldsymbol{0} \le \boldsymbol{g}(\boldsymbol{q}, \boldsymbol{k} \mid \boldsymbol{L}_{\text{val}}, \boldsymbol{U}_{\text{val}}) \\ &\boldsymbol{0} = \boldsymbol{h}(\boldsymbol{q}, \boldsymbol{k}, \boldsymbol{p}, \boldsymbol{f} \mid \Delta p_{\text{pump}}, \tilde{\boldsymbol{k}}_{\text{rad}}, \boldsymbol{d}, \boldsymbol{l}, \boldsymbol{\varepsilon}), \end{aligned} \tag{19}$$

the performance J in Eq. (2) is, using Eq. (15), upper bounded by

$$J(\boldsymbol{k}_{\text{val}}) \le L\left(\boldsymbol{q}_{\text{rad}}\right) \lim_{T \to \infty} \frac{1}{T} \int_0^T \mathcal{I}(t)\, dt, \tag{20}$$

and $\mathcal{I}(t)$ is given by Eq. (16). Since the upper bound in Eq. (20) is scaled by the performance proxy $L(\boldsymbol{q}_{\text{rad}})$, L can be used to assess how the valve configurations $\boldsymbol{k}_{\text{val}}$ affect the upper bound of the performance J via the Eq. (19).

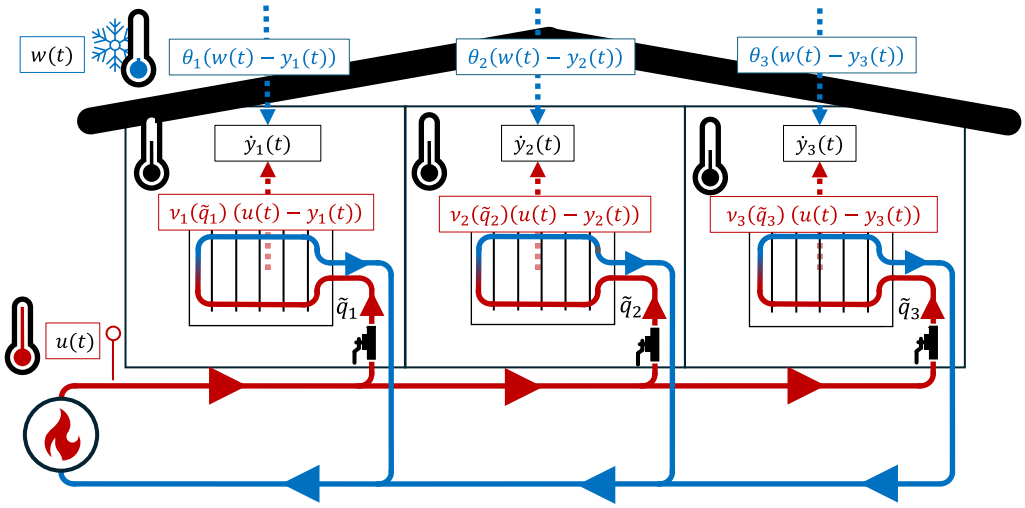

Fig. 2. Schematic overview of the thermal model for a heating system of $Z = 3$ thermal zones, corresponding to Fig. 1. The pump, which is located close to the heat source, is omitted in this view.

From Eq. (18), the performance proxy L can be rewritten as

$$\begin{aligned} L(\boldsymbol{q}_{\text{rad}}) &= \|\boldsymbol{\theta}\|_2^2 - 2\frac{(\boldsymbol{\theta}^\top \boldsymbol{\nu}(\boldsymbol{q}_{\text{rad}}))^2}{\|\boldsymbol{\nu}(\boldsymbol{q}_{\text{rad}})\|_2^2} + \frac{(\boldsymbol{\theta}^\top \boldsymbol{\nu}(\boldsymbol{q}_{\text{rad}}))^2 \|\boldsymbol{\nu}(\boldsymbol{q}_{\text{rad}})\|_2^2}{\|\boldsymbol{\nu}(\boldsymbol{q}_{\text{rad}})\|_2^4} \\ &= \|\boldsymbol{\theta}\|_2^2 - \frac{(\boldsymbol{\theta}^\top \boldsymbol{\nu}(\boldsymbol{q}_{\text{rad}}))^2}{\|\boldsymbol{\nu}(\boldsymbol{q}_{\text{rad}})\|_2^2} \\ &= \|\boldsymbol{\theta}\|_2^2 - \frac{\|\boldsymbol{\theta}\|_2^2 \|\boldsymbol{\nu}(\boldsymbol{q}_{\text{rad}})\|_2^2 \cos^2\varphi}{\|\boldsymbol{\nu}(\boldsymbol{q}_{\text{rad}})\|_2^2} \\ &= \|\boldsymbol{\theta}\|_2^2 (1 - \cos^2\varphi) \\ &= \|\boldsymbol{\theta}\|_2^2 \sin^2\varphi, \end{aligned} \tag{21}$$

where φ is the angle between the vectors $\boldsymbol{\theta}$ and $\boldsymbol{\nu}(\boldsymbol{q}_{\text{rad}})$. The last row in Eq. (21) may provide intuition on how the flow rates $\boldsymbol{q}$ ideally should be set: the vector of heat supply coefficients $\boldsymbol{\nu}(\boldsymbol{q}_{\text{rad}})$ and the vector of thermal leakage coefficients $\boldsymbol{\theta}$ should be aligned so that the angle φ is the smallest possible. Although it is generally not achievable, the ideal scenario would be to obtain $\varphi = 0$ such that $\boldsymbol{\theta}$ and $\boldsymbol{\nu}(\boldsymbol{q}_{\text{rad}})$ are parallel and the reference temperature y_{ref} can be maintained in all zones, irrespective of outdoor temperature w.

4. Guidance for rebalancing using operational data

With a traditional balancing approach, data from the construction plan is used to calculate valve settings and flow rates without taking into account an observed state of balancing in the thermal zones. Therefore, a traditional approach can not instruct how to rebalance the flow rates to correct for observed misalignments that are not connected to updates in the construction plan. This section describes tools, based on the modeling in Section 3, in which collected operational data, as specified in Section 2, is used to facilitate informed decisions of rebalancing. In Section 4.1, it is described how coefficients needed for calculating the balancing performance proxy $L(\tilde{\boldsymbol{q}}_{\text{rad}})$ in Eq. (18) under fixed radiator flow rates $\tilde{\boldsymbol{q}}_{\text{rad}}$ are collected by the means of the construction plan and the sensor data. Based on those coefficients, bounds of the performance obtained from a rebalancing $\Delta\boldsymbol{q}_{\text{rad}}$, the *post-rebalanced performance proxy* $L(\tilde{\boldsymbol{q}}_{\text{rad}} + \Delta\boldsymbol{q}_{\text{rad}})$ are derived in Section 4.2. The bounds of the post-rebalanced performance proxy enable anticipating the effect of a given rebalancing $\Delta\boldsymbol{q}_{\text{rad}}$, but it also provides an opportunity to calculate an optimized rebalancing $\Delta\boldsymbol{q}_{\text{rad}}$, which is described in Section 4.3.

4.1. Determining model coefficients

The data sources from the problem formulation in Section 2 are the balancing protocol, which gives flow rates $\tilde{\boldsymbol{q}}$ and valve configurations $\tilde{\boldsymbol{k}}_{\text{val}}$, the construction plan, which gives the pipe characteristics of diameters $\boldsymbol{d}$, lengths $\boldsymbol{l}$, and roughnesses $\boldsymbol{\varepsilon}$, and the sampled operational data, which gives time-series of the zone air temperatures $\boldsymbol{y}$, supply temperature u, and outdoor temperature w sampled with a period of Δt.

To set up the hydraulic model in Eq. (6), the pump's differential pressure Δp_{pump} is retrieved from the setting of the pump, the lower and upper bounds of the valve clamping capacities $\boldsymbol{L}_{\text{val}}$ and $\boldsymbol{U}_{\text{val}}$ are retrieved from the data sheets of the installed valves, the pipe characteristics $\boldsymbol{d}$, $\boldsymbol{l}$, and $\boldsymbol{\varepsilon}$ are retrieved from the construction plan. The constant radiator resistances $\tilde{\boldsymbol{k}}_{\text{rad}}$, used in Eq. (5b), are selected such that the flow rates $\tilde{\boldsymbol{q}}$ and valve configuration $\tilde{\boldsymbol{k}}_{\text{val}}$ forms a feasible solution in Eq. (6)

$$\begin{aligned} \mathbf{0} &\le \boldsymbol{g}(\tilde{\boldsymbol{q}}, \tilde{\boldsymbol{k}} \mid \boldsymbol{L}_{\text{val}}, \boldsymbol{U}_{\text{val}}) \\ \mathbf{0} &= \boldsymbol{h}(\tilde{\boldsymbol{q}}, \tilde{\boldsymbol{k}}, \tilde{\boldsymbol{p}}, \tilde{\boldsymbol{f}} \mid \Delta p_{\text{pump}}, \tilde{\boldsymbol{k}}_{\text{rad}}, \boldsymbol{d}, \boldsymbol{l}, \boldsymbol{\varepsilon}). \end{aligned} \tag{22}$$

where the flow rates $\tilde{\boldsymbol{q}}$, valve configurations $\tilde{\boldsymbol{k}}_{\text{val}}$ are retrieved from the balancing protocol. The pipes' friction factors $\tilde{\boldsymbol{f}}$ and resistances $\tilde{\boldsymbol{k}}_{\text{pip}}$ are retrieved by inserting the known values for $\tilde{\boldsymbol{q}}$, $\tilde{\boldsymbol{k}}_{\text{rad}}$, $\boldsymbol{d}$, $\boldsymbol{l}$, and $\boldsymbol{\varepsilon}$ in Eq. (5c) and (5d). Given these values of $\tilde{\boldsymbol{k}}_{\text{val}}$ and $\tilde{\boldsymbol{k}}_{\text{pip}}$, the pressures $\tilde{\boldsymbol{p}}$ can then be calculated from Eq. (4c), (4d), and (4d) since there is only one radiator per flow path from $b = 1$ to $b = B$ in a two-pipe system. Given $\tilde{\boldsymbol{p}}$ and $\tilde{\boldsymbol{q}}_{\text{rad}}$, there is a unique vector $\tilde{\boldsymbol{k}}_{\text{rad}}$ satisfying Eq. (4c) for radiator edges $a = 1, \dots, R$.

The operational data, collected under the current flow rates $\tilde{\boldsymbol{q}}_{\text{rad}}$, is used to determine the thermal coefficient of the thermal leakage $\boldsymbol{\theta}$ and the heat supply $\boldsymbol{\nu}(\tilde{\boldsymbol{q}}_{\text{rad}})$, which appear in the performance proxy L in Eq. (18). The coefficient estimates $\hat{\boldsymbol{\theta}}$ and $\hat{\boldsymbol{\nu}}(\tilde{\boldsymbol{q}}_{\text{rad}})$ are fitted to the discretized dynamics of Eq. (11),

$$\frac{\boldsymbol{y}(t+\Delta t) - \boldsymbol{y}(t)}{\Delta t} = \text{diag}(\boldsymbol{\theta})\,(\mathbb{1}\, w(t) - \boldsymbol{y}(t)) + \text{diag}(\boldsymbol{\nu})\,(\mathbb{1}\, u(t) - \boldsymbol{y}(t)). \tag{23}$$

4.2. Bounds of the post-rebalanced performance proxy

From the expression for the performance proxy L in Eq. (18), evaluation of the post-rebalanced performance proxy $L(\tilde{\boldsymbol{q}}_{\text{rad}} + \Delta\boldsymbol{q}_{\text{rad}})$ requires the corresponding values of the rebalanced heat supply coefficient $\boldsymbol{\nu}(\tilde{\boldsymbol{q}}_{\text{rad}} + \Delta\boldsymbol{q}_{\text{rad}})$. Although the heat supply coefficient $\boldsymbol{\nu}(\tilde{\boldsymbol{q}}_{\text{rad}})$ is estimated, the operational data with constant flow rates $\tilde{\boldsymbol{q}}_{\text{rad}}$ does not allow for uniquely determining the underlying C_z, L_z m_z in Eq. (10). Consequently, rebalanced heat supply coefficient $\boldsymbol{\nu}(\tilde{\boldsymbol{q}}_{\text{rad}} + \Delta\boldsymbol{q}_{\text{rad}})$ can not be

assigned with a unique value, but it can be bounded as justified in this section.

Given a positive C_z from Eqs. (7) and (10) gives

$$\begin{aligned} v_z(0) &= 0 \\ 0 &< v_z'(q_{\text{zon},z}) \\ v_z''(q_{\text{zon},z}) &< 0, \end{aligned} \tag{24}$$

which is shown in Appendix B. Thus, v_z is monotonically increasing and concave in $q_{\text{zon},z}$. The positive derivative $0 < v_z'$ means that the radiators' heating power $\Phi_{P_z:R_Z}$ increases with the zonal flow rate $q_{\text{zon},z}$, and the negative second derivative $v_z'' \leq 0$ corresponds to a return temperature that increases with the flow rate $q_{\text{zon},z}$, which is explained in more detail in Appendix B.

The properties in Eq. (24) gives the lower and upper bounds

$$\begin{cases} v_z(\tilde{q}_{\text{zon},z} + \Delta q_{\text{zon},z}) \in \left[v_z(\tilde{q}_{\text{zon},z}) + \Delta q_{\text{zon},z} \dfrac{v_z(\tilde{q}_{\text{zon},z})}{\tilde{q}_{\text{zon},z}}, \right. \\ \left. v_z(\tilde{q}_{\text{zon},z}) \right], \text{if } \Delta q_{\text{zon},z} \in \left[-\tilde{q}_{\text{zon},z}, 0 \right], \\ v_z(\tilde{q}_{\text{zon},z} + \Delta q_{\text{zon},z}) \in \left[v_z(\tilde{q}_{\text{zon},z}), \right. \\ \left. v_z(\tilde{q}_{\text{zon},z}) + \Delta q_{\text{zon},z} \dfrac{v_z(\tilde{q}_{\text{zon},z})}{\tilde{q}_{\text{zon},z}} \right], \text{if } \Delta q_{\text{zon},z} \in [0, \infty). \end{cases} \tag{25}$$

where

$$\Delta q_{\text{zon},z} = \sum_{r=P_z}^{R_z} \Delta q_{\text{rad},r} \tag{26}$$

is the total flow rate change in zone z. The derivation of Eq. (25) is given in Appendix B. Based on the bounds in Eq. (25), we formulate the possible values for the heat supply coefficient of all zones $\boldsymbol{\nu}(\tilde{\boldsymbol{q}}_{\text{rad}} + \Delta \boldsymbol{q}_{\text{rad}})$ as obtained after a flow rate redistribution $\Delta \boldsymbol{q}_{\text{rad}}$ with the set

$$\boldsymbol{\nu}(\tilde{\boldsymbol{q}}_{\text{rad}} + \Delta \boldsymbol{q}_{\text{rad}}) \in \{ \boldsymbol{\nu}(\tilde{\boldsymbol{q}}_{\text{rad}}) + \boldsymbol{\eta}(\Delta \boldsymbol{q}_{\text{rad}}, \boldsymbol{\alpha} \mid \tilde{\boldsymbol{q}}_{\text{rad}}) \mid \boldsymbol{\alpha} \in [0,1]^N \} \tag{27}$$

where $\boldsymbol{\alpha} \in [0,1]^N$ is a parameter for describing the possible outcomes,

$$\boldsymbol{\eta}(\Delta \boldsymbol{q}_{\text{rad}}, \boldsymbol{\alpha} \mid \tilde{\boldsymbol{q}}_{\text{rad}}) = [\eta(\Delta q_{\text{zon},1}, \alpha_1 \mid \tilde{q}_{\text{zon},1}), \ldots, \eta(\Delta q_{\text{zon},Z}, \alpha_Z \mid \tilde{q}_{\text{zon},Z})]^\top \tag{28}$$

and

$$\eta(\Delta q_{\text{zon},z}, \alpha_z \mid \tilde{q}_{\text{zon},z}) = \alpha_z \Delta q_{\text{zon},z} \frac{v_z(\tilde{q}_{\text{zon},z})}{\tilde{q}_{\text{zon},z}}. \tag{29}$$

An example of the set in Eq. (27), but for one of the zones, is depicted in Fig. 3.

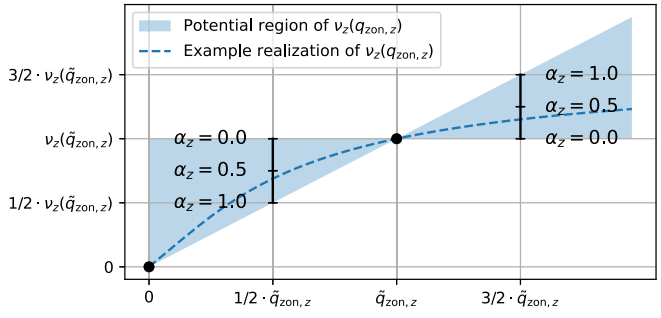

Fig. 3. Example of the bounds of $v_z(\tilde{q}_{\text{zon},z} + \Delta q_{\text{zon},z})$ as described by Eq. (27), for one zone z. Black dots denote the known values of $v_z(0) = 0$ and $v_z(\tilde{q}_{\text{zon},z})$. The left vertical line shows $\alpha_z = 0, 0.5, 1$ corresponding to a flow rate decrease of $\Delta q_{\text{zon},z} = -\frac{1}{2}\tilde{q}_{\text{zon},z}$, and the right vertical line shows the same for a flow rate increase $\Delta q_{\text{zon},z} = \frac{1}{2}\tilde{q}_{\text{zon},z}$.

Given the set in Eq. (27), the post-rebalanced performance proxy is bounded by

$$L_{\text{bc}}(\Delta \boldsymbol{q}_{\text{rad}} \mid \tilde{\boldsymbol{q}}_{\text{rad}}, \boldsymbol{\theta}) \leq L(\tilde{\boldsymbol{q}}_{\text{rad}} + \Delta \boldsymbol{q}_{\text{rad}}) \leq L_{\text{wc}}(\Delta \boldsymbol{q}_{\text{rad}} \mid \tilde{\boldsymbol{q}}_{\text{rad}}, \boldsymbol{\theta}) \tag{30}$$

where L_{bc} is the *best-case post-rebalanced performance proxy*

$$L_{\text{bc}}(\Delta \boldsymbol{q}_{\text{rad}} \mid \tilde{\boldsymbol{q}}_{\text{rad}}, \boldsymbol{\theta}) = \min_{\boldsymbol{\alpha}_{\text{bc}} \in [0,1]^N} \|\boldsymbol{\theta}\|_2^2 - \frac{(\boldsymbol{\theta}^\top (\boldsymbol{\nu}(\tilde{\boldsymbol{q}}_{\text{rad}}) + \boldsymbol{\eta}(\Delta \boldsymbol{q}_{\text{rad}}, \boldsymbol{\alpha}_{\text{bc}} \mid \tilde{\boldsymbol{q}}_{\text{rad}})))^2}{\|\boldsymbol{\nu}(\tilde{\boldsymbol{q}}_{\text{rad}}) + \boldsymbol{\eta}(\Delta \boldsymbol{q}_{\text{rad}}, \boldsymbol{\alpha}_{\text{bc}} \mid \tilde{\boldsymbol{q}}_{\text{rad}})\|_2^2}, \tag{31}$$

and L_{wc} is the *worst-case post-rebalanced performance proxy*

$$L_{\text{wc}}(\Delta \boldsymbol{q}_{\text{rad}} \mid \tilde{\boldsymbol{q}}_{\text{rad}}, \boldsymbol{\theta}) = \max_{\boldsymbol{\alpha}_{\text{wc}} \in [0,1]^N} \|\boldsymbol{\theta}\|_2^2 - \frac{(\boldsymbol{\theta}^\top (\boldsymbol{\nu}(\tilde{\boldsymbol{q}}_{\text{rad}}) + \boldsymbol{\eta}(\Delta \boldsymbol{q}_{\text{rad}}, \boldsymbol{\alpha}_{\text{wc}} \mid \tilde{\boldsymbol{q}}_{\text{rad}})))^2}{\|\boldsymbol{\nu}(\tilde{\boldsymbol{q}}_{\text{rad}}) + \boldsymbol{\eta}(\Delta \boldsymbol{q}_{\text{rad}}, \boldsymbol{\alpha}_{\text{wc}} \mid \tilde{\boldsymbol{q}}_{\text{rad}})\|_2^2}. \tag{32}$$

Since $\boldsymbol{\alpha}_{\text{bc}} = \mathbf{0}$ gives an upper bound of Eq. (31), the best-case post-rebalanced performance proxy is upper bounded by

$$L_{\text{bc}}(\Delta \boldsymbol{q}_{\text{rad}} \mid \tilde{\boldsymbol{q}}_{\text{rad}}, \boldsymbol{\theta}) \leq L(\tilde{\boldsymbol{q}}_{\text{rad}}), \tag{33}$$

and since $\boldsymbol{\alpha}_{\text{wc}} = \mathbf{0}$ gives a lower bound of Eq. (32) the worst-case post-rebalanced performance proxy is lower bounded by

$$L(\tilde{\boldsymbol{q}}_{\text{rad}}) \leq L_{\text{wc}}(\Delta \boldsymbol{q}_{\text{rad}} \mid \tilde{\boldsymbol{q}}_{\text{rad}}, \boldsymbol{\theta}). \tag{34}$$

In other words, the best-case post-rebalanced performance proxy $L_{\text{bc}}(\Delta \boldsymbol{q}_{\text{rad}})$ cannot be worse than the pre-rebalanced performance proxy $L(\tilde{\boldsymbol{q}}_{\text{rad}})$ and the worst-case post-rebalanced performance proxy $L_{\text{wc}}(\Delta \boldsymbol{q}_{\text{rad}})$ cannot be better than the pre-rebalanced performance proxy $L(\tilde{\boldsymbol{q}}_{\text{rad}})$.

Given a suggested flow rate rebalancing $\Delta \boldsymbol{q}_{\text{rad}}$, the outcome by applying $\Delta \boldsymbol{q}_{\text{rad}}$ can be anticipated in advance through the worst-case and best-case performance proxies L_{wc} and L_{bc}. Thus, a technician can be informed whether the suggested rebalancing $\Delta \boldsymbol{q}_{\text{rad}}$ has any improvement potential at all, and compare it with other candidate rebalancings.

4.3. Optimization of valve reconfigurations

In simple heating systems, such as the toy example in Figs. 1 and 2, it might be possible to rebalance flow rates such that $\Delta \boldsymbol{q}_{\text{rad}} \neq \mathbf{0}$ with $L_{\text{bc}}(\Delta \boldsymbol{q}_{\text{rad}}) < L(\tilde{\boldsymbol{q}}_{\text{rad}}) = L_{\text{wc}}(\Delta \boldsymbol{q}_{\text{rad}})$, i.e., the performance proxy will for sure not be worsened. It is, however, common to have nested pipe structures and non-ideal sizing of valves and pumps, such that the hydraulics in Eq. (6) will constrain how flow rates can be rebalanced. Under such circumstances, the best-case performance proxy L_{bc} and worst-case performance proxy L_{wc} may be conflicting, i.e., to get a small best-case performance proxy L_{bc} we might simultaneously also have to take a risk with a large worst-case performance L_{wc}.

A valve reconfiguration $\tilde{\boldsymbol{k}}_{\text{val}} + \Delta \boldsymbol{k}_{\text{val}}$, producing the rebalanced radiator flow rates $\tilde{\boldsymbol{q}}_{\mathbf{rad}} + \Delta \boldsymbol{q}_{\text{rad}}$, that corresponds to a Pareto-optimal solution of worst-case L_{wc} and baset-case L_{bc} is retrieved by

$$\begin{aligned} &\underset{\Delta \boldsymbol{k}, \Delta \boldsymbol{q}, \boldsymbol{p}, \boldsymbol{f}}{\text{minimize}} \; \zeta L_{\text{bc}}(\Delta \boldsymbol{q}_{\text{rad}} \mid \tilde{\boldsymbol{q}}_{\text{rad}}, \boldsymbol{\theta}) \\ &\quad + (1 - \zeta) L_{\text{wc}}(\Delta \boldsymbol{q}_{\text{rad}} \mid \tilde{\boldsymbol{q}}_{\text{rad}}, \boldsymbol{\theta}) \end{aligned} \tag{35a}$$

subject to

$$\mathbf{0} \leq \boldsymbol{g}(\tilde{\boldsymbol{q}} + \Delta \boldsymbol{q}, \tilde{\boldsymbol{k}} + \Delta \boldsymbol{k} \mid \boldsymbol{L}_{\text{val}}, \boldsymbol{U}_{\text{val}}) \tag{35b}$$

$$\mathbf{0} = \boldsymbol{h}(\tilde{\boldsymbol{q}} + \Delta \boldsymbol{q}, \tilde{\boldsymbol{k}} + \Delta \boldsymbol{k}, \boldsymbol{p}, \boldsymbol{f} \mid \Delta p_{\text{pump}}, \tilde{\boldsymbol{k}}_{\text{rad}}, \boldsymbol{d}, \boldsymbol{l}, \boldsymbol{\varepsilon}) \tag{35c}$$

where the objective function in Eq. (35a) is sum of L_{bc} in Eq. (31) and L_{wc} in Eq. (32) weighted by the parameter $\zeta \in [0,1]$, Eqs. (35b) and (35c) are inequalities and equations from the hydraulic model in Eq. (6) set up as described in Section 4.1.

With a small ζ in Eq. (35a), minimizing the risk from the worst-case performance is prioritized over enabling a low best-case performance L_{bc}. Conversely, a large ζ corresponds to risking a high worst-case performance L_{wc} to prioritize a low best-case performance L_{bc}. By knowing a preferred risk level ζ, the optimal valve reconfiguration $\Delta \boldsymbol{k}_{\text{val}}$ can be

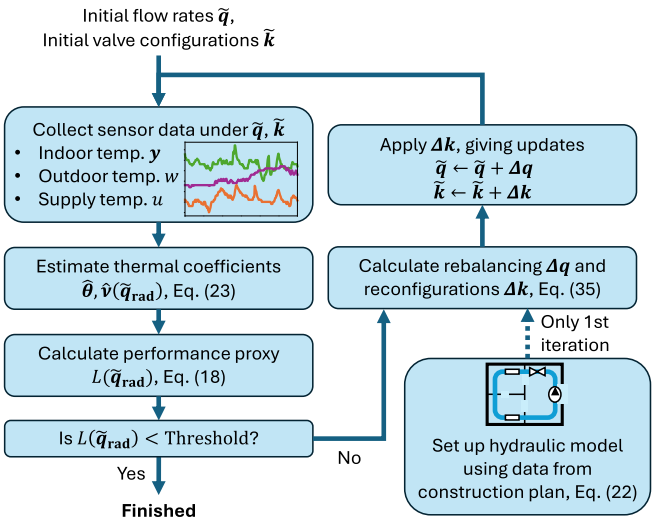

Fig. 4. Overview of an iterative workflow using the model-based tools for evaluation and reconfiguration guidance presented in this paper.

obtained by Eq. (35). However, interpreting the effect of the weighting parameter ζ in advance may be difficult to do beforehand, and a more convenient approach is to calculate multiple Pareto-optimal solutions by varying the weighting parameter ζ and then select a rebalancing Δq_{rad} which correspond to a desired point at the Pareto front.

Altogether, the reconfiguration guidance can be combined with the evaluation based on the performance proxy $L(q_{rad})$ in Eq. (18) in an iterative manner, as illustrated in Fig. 4. In a full adoption of the proposed framework, rebalancing would be repeated until the performance proxy $L(q_{rad})$ falls below a predefined threshold. After each iteration, new operational data must be collected to refit the thermal coefficients in Eq. (23). This implies a trade-off: longer waiting times between iterations provide more data and thus more reliable estimates, but also delay the rebalancing process. By contrast, the hydraulic model remains unchanged once it has been set up, unless modifications to the construction plan are introduced.

5. Case study

In this section, data from before and after the rebalancing of a heating system on February 7, 2024, is used to analyze the applicability of the methods described in Sections 3 and 4. While the tools presented in this work were not directly used for assisting the rebalancing, they are used here to assess the outcome of the rebalancing and to retrospectively find whether there would have been other, more favorable reconfigurations.

5.1. Description of the heating system and balancing work

The heating system, which is visualized in Fig. 5, is a two-pipe system connected to the city's district heating grid via the substation, where the district heating water heats the supply water through a heat exchanger. From the heat exchanger, the supply water is led through the pump and into the main pipe that leads through the basement. The radiators are connected to the main pipe via vertical risers so that radiators located at a similar position but on different floors share the same riser.

There are 70 apartments of varying sizes, from 33 - 100 m^2, between one and four rooms. Each apartment has 1 - 5 radiators, depending on the apartment size, and the air temperature is measured from a sensor mounted close to the entrance. Since there is only one temperature sensor per apartment, each apartment is treated as a single thermal zone in the remainder of the analysis.

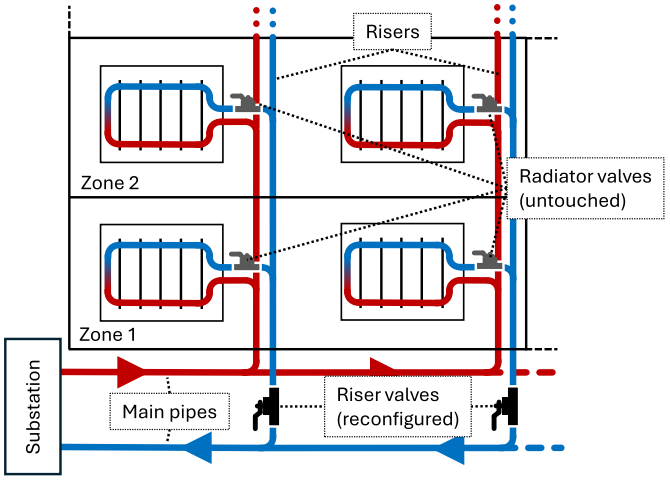

Fig. 5. Schematic of the structure of the pipe system in the case study.

In addition to balancing valves on each radiator, there are balancing valves at the bottom of the return pipe of each riser, *riser valves*, before its junction with the main return pipe. Therefore, the configuration of one riser valve affects multiple radiators on different floors. The apartments connected to a single riser differ in size, flor plan and window direction. The riser valves are easy to access since they are all mounted on the main pipe in the basement, while access to the radiator valves requires permission from the tenants.

Before the rebalancing on February 7, 2024, the heating system underwent thorough balancing work in 2020 and 2021, when both radiator and riser valves were configured according to a flow rate protocol, as given by an ordinary balancing calculation based on construction plan data. When the balancing work finished in 2021, the TRVs were remounted on all radiators. Still, the zone temperature variance was high in the succeeding years 2022 - 2024. It was observed that many zones had a similar climate to the other zones connected to the same riser, and simultaneously disparate from zones connected to other risers. Therefore, reconfiguration of riser valves was identified as an appropriate measure to mitigate temperature variance. However, since there were no updates in the construction plan since 2021, redoing the balancing procedure from scratch would just result in the same valve configurations. Instead, the riser valves were reconfigured to increase the flow rate in risers serving zones assessed to be underheated and decrease it in other overheated zones. 10 of 61 riser valves underwent reconfiguration in February 2024, affecting 16 of 70 apartments. To not affect the pump's operating condition and the other valves, the total flow rate was aimed to be kept intact by compensating for the increased flow rate at one valve with the decreased flow rate at the other valves.

5.2. Analysis of the rebalancing outcome

Given the flow rates $\tilde{q}_{rad}$, a successful rebalancing Δq_{rad} should modify the heat supply coefficients ν such that the reduced performance proxy L is reduced as, using Eq. (21),

$$\begin{aligned} & L(\tilde{q}_{rad} + \Delta\tilde{q}_{rad}) < L(\tilde{q}_{rad}) \\ \iff & \\ \|\theta\|_2^2 - \frac{(\theta^\top \nu(\tilde{q}_{rad} + \Delta q_{rad}))^2}{\|\nu(\tilde{q}_{rad} + \Delta q_{rad})\|_2^2} & < \|\theta\|_2^2 - \frac{(\theta^\top \nu(\tilde{q}_{rad}))^2}{\|\nu(\tilde{q}_{rad})\|_2^2} \\ \iff & \\ \|\theta\|_2^2 \sin^2 \varphi_{post} & < \|\theta\|_2^2 \sin^2 \varphi_{pre} \\ \implies & \\ \varphi_{post} & < \varphi_{pre} \end{aligned} \tag{36}$$

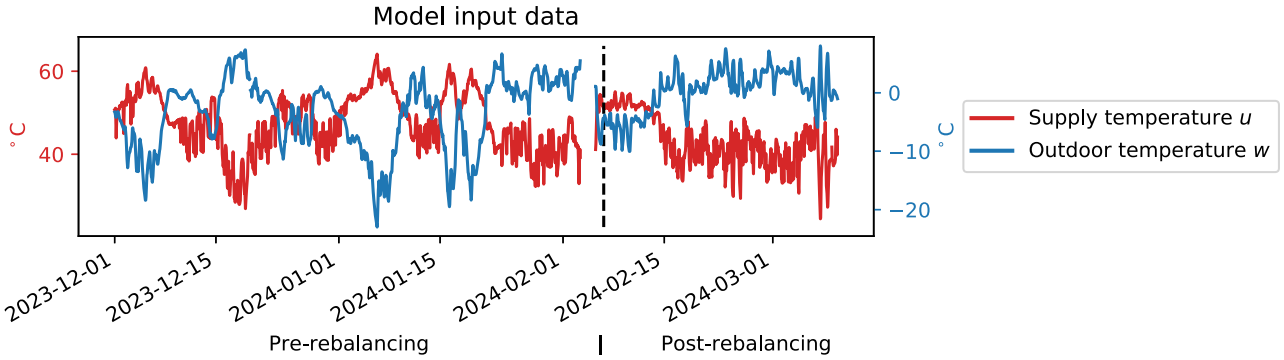

Fig. 6. Dynamic model input signals, supply temperature u and outdoor temperature w, collected from the operation during pre- and post-rebalancing periods. The signals are negatively correlated such that u is higher when w is lower.

where φ_{pre} is the angle between $\boldsymbol{\theta}$ and the pre-rebalanced heat supply coefficients $\boldsymbol{\nu}(\tilde{\boldsymbol{q}}_{\text{rad}})$ and φ_{post} is the angle between $\boldsymbol{\theta}$ and the post-rebalanced heat supply coefficients $\boldsymbol{\nu}(\tilde{\boldsymbol{q}}_{\text{rad}} + \Delta\boldsymbol{q}_{\text{rad}})$. The last row in Eq. (36) underlines that with this modeling, a rebalancing $\Delta\boldsymbol{q}_{\text{rad}}$ will not affect the performance proxy L through the norm of the thermal leakage coefficients $\|\boldsymbol{\theta}\|_2^2$ but through the angle φ calculated by

$$\varphi = \arccos\left(\frac{\boldsymbol{\theta}^{\top}\boldsymbol{\nu}}{\|\boldsymbol{\nu}\|_2\,\|\boldsymbol{\theta}\|_2}\right), \tag{37}$$

given coefficients $\boldsymbol{\theta}$ and $\boldsymbol{\nu}$.

To analyze the outcome of the rebalancing $\Delta\boldsymbol{q}_{\text{rad}}$ in terms of the angle φ, values of the thermal leakage $\boldsymbol{\theta} \in \mathbb{R}^Z$ and the heat supply $\boldsymbol{\nu} \in \mathbb{R}^Z$ are estimated by fitting of the discretized dynamics in Eq. (23) to the operational data sampled with a period of $\Delta t = 1$ hour. To estimate the pre-rebalanced angle $\hat{\varphi}_{\text{pre}}$, coefficients $\hat{\boldsymbol{\theta}}_{\text{pre}}$ and $\hat{\boldsymbol{\nu}}_{\text{pre}}(\tilde{\boldsymbol{q}})$ are fitted to data from a pre-rebalancing period December 1st 2023 - February 7, 2024, and to estimate the post-rebalanced angle $\hat{\varphi}_{\text{post}}$ coefficients $\hat{\boldsymbol{\theta}}_{\text{post}}$ and $\hat{\boldsymbol{\nu}}_{\text{post}}(\tilde{\boldsymbol{q}}_{\text{rad}} + \Delta\boldsymbol{q}_{\text{rad}})$ are fitted to data from a post-rebalancing period February 7, 2024 - March 10, 2024.

In both pre- and post-rebalancing periods, the data is collected during normal system operation, when the controlled supply temperature u is negatively correlated with the outdoor temperature w, which can be seen in the middle row in Fig. 6. Such a control strategy is suitable to maintain a small error norm $\|\boldsymbol{e}\|_2^2$, as described in Section 3.3, but it makes identification challenging since the correlated signals cause estimation variance of fitted coefficients $\hat{\boldsymbol{\theta}}$ and $\hat{\boldsymbol{\nu}}$. To ensure that physically realistic coefficients $\hat{\boldsymbol{\theta}}$ and $\hat{\boldsymbol{\nu}}$ are obtained, a Bayesian regression approach is used with a Gaussian prior on the thermal leakage

$$\theta_z \sim \mathcal{N}(\mu_\theta, \sigma_\theta^2) \tag{38}$$

for each zone $z = 1, \ldots, Z$. Earlier studies of Swedish residential buildings have found time constants ranging from 4 - 12 days for multi-family buildings [34]. The time constant corresponds to $1/\theta_z$ of the thermal dynamics in Eq. (7), and the hyperparameters in the Gaussian prior Eq. (38), μ_θ and σ_θ^2, are selected such that $\mu \pm 3\sigma$, i.e., 99.7 % of the probability mass, of the prior covers time constants 4 - 12 days. For the heat supply coefficients $\boldsymbol{\nu}$, a flat prior is used.

The zone temperature variance is varying in time, with the supply temperature u and the outdoor temperature w, which can be seen by comparing Figs. 6 and 7. Fig. 7 also shows that such a time-varying variance is obtained when simulating zone temperatures using the obtained maximum aposteriori (MAP) coefficients $\hat{\boldsymbol{\theta}}$ and $\hat{\boldsymbol{\nu}}$, although the variance is underestimated at several occasions. The MAP estimates of the time constants $1/\hat{\theta}_z$, for $z = 1, \ldots, Z$ are around 6 days for all zones.

Based on the fitted coefficients, the pre- and post-rebalanced angles φ_{pre} and φ_{post} are calculated for four groups of thermal zones: *the intervened zones*, which are the $Z = 16$ zones affected by the rebalancing, and three groups of *non-intervened zones*, of which each group consists of $Z = 16$ zones not affected by the rebalancing. With coefficients $\boldsymbol{\theta}$ and $\boldsymbol{\nu}$ sampled from posterior distribution, Table 1 and Fig. 8 indicate some degree of uncertainty in the results, but the posterior probability for a decreased angle $\varphi_{\text{post}} < \varphi_{\text{pre}}$ is substantially higher for the intervened zones than for any non-intervened group. For the three non-intervened groups, and particularly non-intervened group II, the results in Fig. 8 suggest $\varphi_{\text{pre}} < \varphi_{\text{post}}$, i.e., worsened balancing performance, with a high posterior probability.

Table 1
The first and second columns show the estimated pre- and post-rebalanced angles where the first number in each cell correspond to the MAP estimate, and the range corresponds to a 99 % credibility interval. The third column show the posterior probability for a angle decrease $\varphi_{\text{post}} < \varphi_{\text{pre}}$ following the rebalancing.

	φ_{pre}	φ_{post}	$\mathbb{P}(\varphi_{\text{post}} < \varphi_{\text{pre}})$
Intervened	0.077 ± 0.009	0.069 ± 0.016	0.802
Non-intervened I	0.065 ± 0.010	0.067 ± 0.015	0.263
Non-intervened II	0.058 ± 0.008	0.071 ± 0.015	0.009
Non-intervened III	0.070 ± 0.013	0.076 ± 0.024	0.127

The results of the angles φ_{pre} and φ_{post} from Table 1 and Fig. 8 agrees with the observed temperature variance, visualized in Fig. 9. The variance range is shifted between pre- and post-rebalancing periods for all four groups, which is partly explained by the effect of the time-varying behavior of the variance visualized in Fig. 7. Still, the intervened zones stand out in that the variance is shifted downwards more than for any other group.

5.3. Analysis of the pre-rebalancing options

To demonstrate how the method can assist balancing, the pre-rebalancing coefficients $\hat{\boldsymbol{\theta}}_{\text{pre}}$ and $\hat{\boldsymbol{\nu}}_{\text{pre}}(\tilde{\boldsymbol{q}}_{\text{rad}})$, fitted as described in Section 5.2, are used for calculating the worst-case performance proxy L_{wc} in Eq. (32) and the best-case performance proxy L_{bc} in Eq. (31). Like in Section 5.2, the results here are presented in terms of angles φ_{wc} and φ_{bc} instead of the performance proxies L_{wc} and L_{bc}. The range of φ_{wc} and φ_{bc}, which can be computed before applying a rebalancing, is compared with a Pareto front of φ_{wc}, φ_{bc} for other, non-applied rebalancings $\Delta\boldsymbol{q}_{\text{rad}}$, calculated by solving Eq. (35) given data from the construction plan and balancing protocols as described in Section 4.1, with different weightings ζ.

The results, shown in Fig. 10, indicate that the best-case performance φ_{bc} and the worst-case performance φ_{wc} for the applied rebalancing $\Delta\boldsymbol{q}_{\text{rad}}$ are above the Pareto front. If one of the other rebalancing options on the Pareto front had been chosen instead, the same risk φ_{wc} could be obtained with a better potential φ_{bc}, or vice versa. Nevertheless, one can conclude from Fig. 10 that the applied rebalancing $\Delta\boldsymbol{q}_{\text{rad}}$ is one candidate solution to improve the balancing performance since the best-case angle is better than the pre-rebalanced angle, $\varphi_{\text{bc}} < \varphi_{\text{pre}}$.

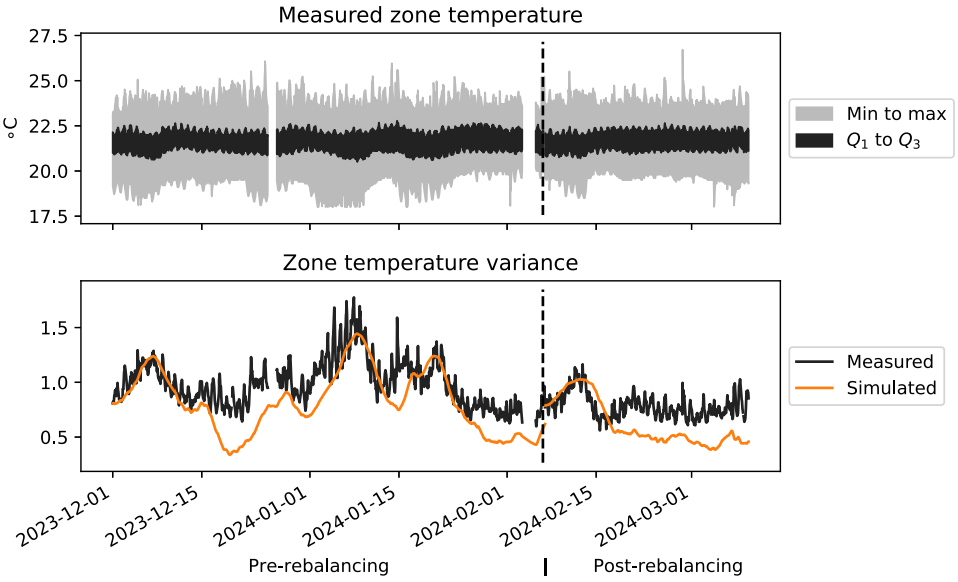

Fig. 7. Comparison of measured and simulated zone temperature variance. The distribution of measured zone temperatures over time is visualized in the upper row, and its variance is indicated in the lower row. The variance of the simulated zone temperatures in the lower row follows the general pattern of the measured variance.

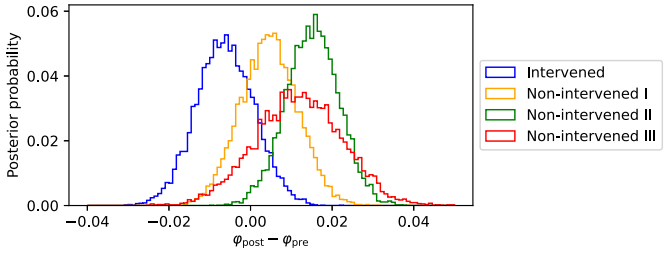

Fig. 8. Posterior probabilities for $\varphi_{post} - \varphi_{pre}$ of the four zone groups. Negative $\varphi_{post} - \varphi_{pre}$ suggests balancing improvement for the intervened zones, while positive or zero-centered $\varphi_{post} - \varphi_{pre}$ suggests preserved or worsened balancing for the non-intervention groups.

In the right-hand plot of Fig. 10, we see that the obtained MAP estimate of the post-rebalanced angle $\hat{\varphi}_{post}$ is in the range $[\varphi_{wc}, \varphi_{bc}]$, demonstrating that the outcome is correctly anticipated. The plot also shows how the width of the interval $[\varphi_{wc}, \varphi_{bc}]$ is, in general, associated with the norm of the rebalancing $\|\Delta \boldsymbol{q}_{rad}\|_2^2$. In other words, a large magnitude of the rebalancing $\|\Delta \boldsymbol{q}_{rad}\|_2^2$ typically means high risk but simultaneously high improvement potential.

6. Discussion

This paper introduces a novel framework for model-based analysis of hydronic balancing, enabling simplification of the balancing process and more effective use of sensor data, as demonstrated in the case study in Section 5. The following discussion reflects both on the potential and the limitations of the proposed methods and results. Specifically, Section 6.1 interprets the results of the case study. Section 6.2 contrasts the proposed framework with conventional approaches, explaining how it can enhance the workflow and be implemented in practice. Finally, Section 6.3 addresses methodological limitations and suggests directions for future work.

6.1. Case study results

The case study demonstrates that the proposed thermal dynamics model can, to a large extent, explain the observed weather-dependent zone temperature variations shown in Fig. 7. The model-based evaluation in Table 1 and Fig. 8 indicates that rebalancing improved performance in the 16 intervened zones, while no such improvement was observed in the groups of non-intervened zones. This result is consistent with the analysis of temperature variation in the pre- and post-rebalancing periods (Fig. 9), where the reduction in variation was more pronounced for the intervened zones. Furthermore, the pre-rebalancing analysis suggested that the applied reconfiguration had improvement potential, although a different configuration strategy might have yielded even greater benefits.

Despite these encouraging results, several uncertainties remain. While the results indicate performance improvements for the intervened zones, the level of uncertainty in the estimates is non-negligible. Analyzing the results strictly even suggests that balancing performance may have been worsened in some non-intervened zones, where no changes should have been applied, potentially indicating that the rebalancing indirectly affected them in adverse ways. Such uncertainties are difficult to eliminate entirely, as the evaluation relies on fitting a model to operational data collected under real-world conditions, where occupancy and human activity inevitably introduce disturbances that may influence the coefficient estimates. Improved experimental design–further discussed in Section 6.3–could mitigate these issues. Ideally, repeated trials would be analyzed through carefully designed comparative experiments, minimizing discrepancies to validate the efficiency of the methods between an intervention group and a control group–for example, using two sets of risers with apartments having very similar characteristics.

6.2. Comparison with a conventional approach

With the conventional practice of rebalancing work, evaluating the outcome is challenging due to the time-varying temperature variance as seen in Fig. 7. Typically, the evaluation is carried out by observing the temperature variance in different weather conditions over a long time, i.e., months or even years. The tools presented in this work provide an opportunity to shorten the cycle time by utilizing the collected sensor data. Rather than directly inspecting the temperature variance, the evaluation can be based on the estimated post-rebalanced angle φ_{post}, as described in Section 5.2, making the process less dependent on specific weather conditions.

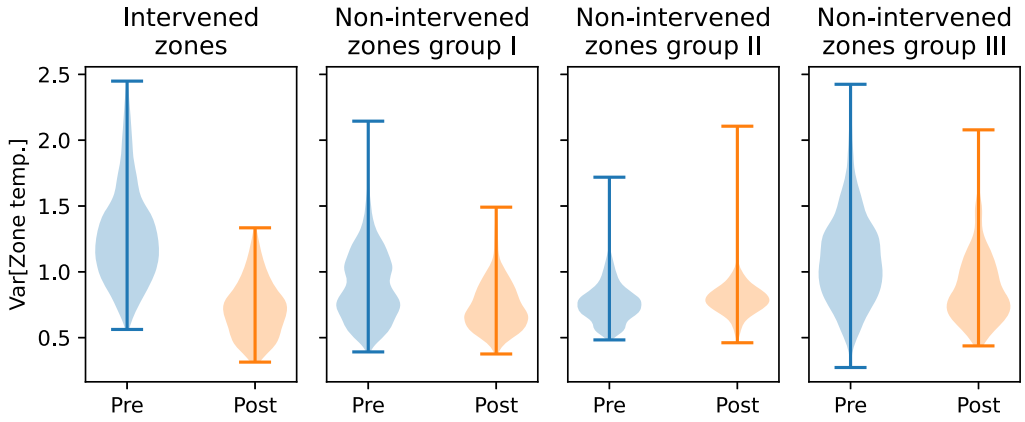

Fig. 9. Distribution of zone temperature variance during the pre- and post-rebalancing periods of four zone groups. The upper and lower range limits for the temperature variance of intervened zones are shifted down more than for any of the groups with non-intervened zones.

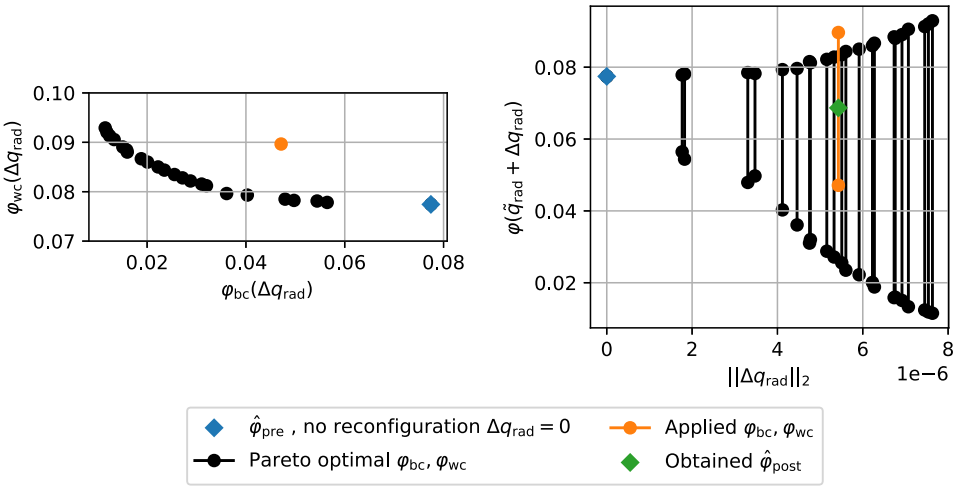

Fig. 10. Visualization of φ_{wc} and φ_{bc} for the applied reconfiguration and the Pareto optimal reconfigurations. The left plot shows that the applied reconfiguration is not Pareto optimal since it is above the Pareto front. The right plot shows that the range in $\varphi_{wc} - \varphi_{bc}$ is associated with the flow rate redistribution norm $\|\Delta \boldsymbol{q}_{rad}\|_2^2$, and that the experimentally obtained MAP estimate $\hat{\varphi}_{post}$ satisfies the pre-rebalancing computed bounds $\varphi_{bc} < \hat{\varphi}_{post} < \varphi_{wc}$.

Furthermore, generating the Pareto front of reconfigurations, as in Section 5.3, enables automated suggestions for how to proceed with the upcoming rebalancing work. The remaining manual work for a technician is to interpret the estimated $\hat{\varphi}_{post}$ to decide whether the rebalancing work should continue, and then possibly reconfigure valves according to a solution from the Pareto front. It should also be emphasized that since temperature sensors are already widespread in Swedish residential heating systems, often no additional equipment is required for employing the tools proposed here.

Although the case study presented here demonstrates the applicability of the methods, it remains an open question whether the proposed approach is more efficient than the educated guesswork performed by technicians using their domain knowledge. To rigorously evaluate this, empirical studies would be needed in which the methods are actively applied by technicians in some systems and compared with other systems where only the conventional approaches are used.

6.3. Limitations of the method

Although the methods presented in this paper enable the utilization of collected sensor data, the main limitation is that the success of the methods requires good data quality. Despite several weeks of estimation data in both pre- and post-rebalancing periods, the posterior distributions of the angle difference $\varphi_{post} - \varphi_{pre}$ fail to provide unambiguous results to the effect of rebalancing, which is due to the uncertainty in $\hat{\theta}$ and $\hat{\nu}$. One approach to improve the reliability and the efficiency of analyzing the rebalancing outcome and calculating new reconfigurations is to design the operation specifically for estimating the thermal coefficients $\boldsymbol{\theta}$ and $\boldsymbol{\nu}$. In the case study, data were collected during normal operation, where the control of the supply temperature u was optimized to maintain indoor comfort. This suggests that improved excitation of u may help to reduce the uncertainty of the coefficient estimates $\hat{\theta}$ and $\hat{\nu}$. Nevertheless, maintaining comfort remains essential, and it is an open question to what extent better excitation of u is implementable and how much the uncertainties can be reduced.

Another limitation is that, although the bounds in Eq. (25) can be established, the post-rebalanced heat supply $\nu(\tilde{\boldsymbol{q}}_{rad} + \Delta \boldsymbol{q}_{rad})$ cannot be calculated exactly prior a rebalancing. This is due to the problem formulation in Section 2, which states that the radiator flow rates $\tilde{\boldsymbol{q}}_{rad}$ are fixed, which correspond to how technicians conventionally collect data and information during balancing work. However, when collecting data under fixed radiator flow rates $\tilde{\boldsymbol{q}}_{rad}$, the coefficients C_z and $L_z \cdot m_z$ in Eq. (A.1) can not be identified. One alternative for future work is that once the radiator flow rates $\tilde{\boldsymbol{q}}_{rad}$ are rebalanced, the coefficients C_z and $L_z \cdot m_z$ can be identified by combining data from pre- and post-rebalancing periods. With such an approach, the post-rebalanced performance proxy $L(\tilde{\boldsymbol{q}}_{rad} + \Delta \boldsymbol{q}_{rad})$ can be calculated directly, eliminating the need for worst- and best-case bounds as given in Section 4.2. Such

and approach is likely more fruitful after several rebalancing iterations, in contrast to the case study in Section 5 which was limited to a single rebalancing event.

7. Conclusions

This paper contributes tools that can guide the balancing work in a structured way while incorporating the operational status through the sensor data. Since the equipment requirements correspond to what is already installed in many Swedish residential heating systems, these methods are widely implementable. The main contribution from this work is a metric for evaluating the performance of flow rate balancing, the performance proxy, in isolation. Unlike relying on zone temperature variance, this evaluation metric is invariant to weather conditions and supply temperature. Furthermore, this framework can be utilized to guide rebalancing, allowing for the calculation of different valve reconfigurations with respect to risk and improvement potential. The case study demonstrates the applicability of these methods, showing that the metrics developed in this work align with the observed zone temperature variance, indicating improved balancing. Also, when only using pre-rebalancing data, the methods suggest that the applied rebalancing had the potential to improve the balancing. However, that analysis also indicates that there were other reconfigurations with even higher potential and lower risk.

CRediT authorship contribution statement

Henrik Håkansson: Writing – original draft, Software, Methodology, Formal analysis, Conceptualization; **Magnus Önnheim:** Writing – review & editing, Supervision, Funding acquisition; **Jonas Sjöberg:** Writing – review & editing, Supervision, Funding acquisition; **Mats Jirstrand:** Writing – review & editing, Supervision, Funding acquisition.

Data availability

The authors do not have permission to share data.

Declaration of competing interest

The authors declare that they have no known competing financial interests or personal relationships that could have appeared to influence the work reported in this paper.

Acknowledgements

This work was financially supported by the Swedish Foundation for Strategic Research (SSF). We also acknowledge Pedram Zadeh, Jonas Tannerstad and Örebrobostäder AB for enabling the case study through active participation and for fruitful discussions.

Appendix A. Derivation of radiator approximation

In this section, we motivate and explain the details of the heat supply approximation as given in Eqs. (8) and (10). For a radiator $r = P_z, \dots, R_z$ in zone z, the heat delivered by the radiator is

$$\Phi_r(t) = c_p\, q_{\text{rad},r}\,(u(t) - T_{\text{r},r}(t)), \tag{A.1}$$

where c_p is the specific heat capacity of water in J / (kg·K), $q_{\text{rad},r}$ is the radiator flow rate, $u(t)$ is the supply temperature in and $T_{\text{r},r}(t)$ is the radiator outlet temperature. To derive an explicit expression for $T_{\text{r},r}$, we model each radiator in zone z as a one-dimensional heat exchanger of length L_z. Since the radiator temperature dynamics are much faster than the indoor air, we consider steady-state radiator temperature dynamics such that the outlet temperature $T_{\text{r},r}$ adapts instantly to changes in the supply temperature $u(t)$ and zone temperature $y_z(t)$. The heat balance equation of an infinitesimal length dx of the radiator with water temperature T is

$$c_p\, q_{\text{rad},r}\, dT = m_z\,(y_z(t) - T)\, dx, \tag{A.2}$$

where m_z is a radiator-specific heat transfer coefficient in W/(K· kg). In practice, the value of the parameter m_z depends on the temperature difference $y_z(t) - T$ [29], although we consider a linearization of the dynamics such that m_z is fixed. Rearranging the terms in Eq. (A.2) gives

$$\frac{m_z}{c_p\, q_z}\, dx = \frac{1}{y_z(t) - T}\, dT, \tag{A.3}$$

and by integrating over the radiator length L_z, and from $u(t)$ to $T_{\text{r},r}$ we get

$$\int_0^{L_z} \frac{m_z}{c_p\, q_z} dx = \int_{u(t)}^{T_{\text{r},r}(t)} \frac{1}{y_z(t) - T} dT \tag{A.4}$$

$$\iff$$

$$\frac{L_z\, m_z}{c_p\, q_{\text{rad},r}} = \log\left(\frac{y_z(t) - u(t)}{y_z(t) - T_{\text{r},r}(t)}\right). \tag{A.5}$$

With

$$K_z = \frac{-L_z\, m_z}{c_p}, \tag{A.6}$$

outlet temperature is

$$T_{\text{r},r}(t) = \exp\left(\frac{K_z}{q_{\text{rad},r}}\right) u(t) + \left(1 - \exp\left(\frac{K_z}{q_{\text{rad},r}}\right)\right) y_z(t) \tag{A.7}$$

and using Eq. (A.1), we can express the heat delivered by radiator r as

$$\begin{aligned}
\Phi_r(t) &= c_p\, q_{\text{rad},r}\left(1 - \exp\left(\frac{K_z}{q_{\text{rad},r}}\right)\right)\big(u(t) - y_z(t)\big) \\
&= c_p\, q_{\text{rad},r}\left(1 - \sum_{n=0}^{\infty} \frac{K_z^n}{q_{\text{rad},r}^n\, n!}\right)\big(u(t) - y_z(t)\big) \\
&= c_p\left(\sum_{n=1}^{\infty} \frac{K_z^n}{q_{\text{rad},r}^{n-1}\, n!}\right)\big(u(t) - y_z(t)\big)
\end{aligned} \tag{A.8}$$

Now, to approximate the total heating power delivered to zone z, $\Phi_{\text{zon},z}$, we denote

$$Q_z = R_z - P_z + 1 \tag{A.9}$$

as the number of radiators in zone z, and use Eq. (8) to (10) and (A.6) to obtain

$$\begin{aligned}
\tilde{\Phi}_{\text{zon},z}(t) &= \frac{1}{C_z}\, \nu_z(q_{\text{zon},z})(u(t) - y_z(t)) \\
&= \frac{C_z}{C_z}\, c_p\, q_{\text{zon},z}\left(1 - \exp\left(\frac{Q_z\, K_z}{q_{\text{zon},z}}\right)\right)(u(t) - y_z(t)) \\
&= c_p\, q_{\text{zon},z}\left(1 - \exp\left(\frac{Q_z\, K_z}{q_{\text{zon},z}}\right)\right)\big(u(t) - y_z(t)\big) \\
&= c_p\, q_{\text{zon},z}\left(1 - \sum_{n=0}^{\infty} \frac{Q_z^n\, K_z^n}{q_{\text{zon},z}^n\, n!}\right)\big(u(t) - y_z(t)\big) \\
&= c_p\left(\sum_{n=1}^{\infty} \frac{Q_z^n\, K_z^n}{q_{\text{zon},z}^{n-1}\, n!}\right)\big(u(t) - y_z(t)\big),
\end{aligned} \tag{A.10}$$

Given the linearized radiator model Eq. (A.8), the error of the single zone approximation in Eq. (A.10) is

$$\begin{aligned}
&\tilde{\Phi}_{\text{zon},z} - \sum_{r=P_z}^{R_z} \Phi_r \\
&= c_p\left(\sum_{n=1}^{\infty} \frac{Q_z^n\, K_z^n}{q_{\text{zon},z}^{n-1}\, n!} - \sum_{r=P_z}^{R_z} \sum_{n=1}^{\infty} \frac{K_z^n}{q_{\text{rad},r}^{n-1}\, n!}\right)\big(u(t) - y_z(t)\big) \\
&= c_p\left(\sum_{n=1}^{\infty} \frac{K_z^n}{n!}\left(\frac{Q_z^n}{q_{\text{zon},z}^{n-1}} - \sum_{r=P_z}^{R_z} \frac{1}{q_{\text{rad},r}^{n-1}}\right)\right)\big(u(t) - y_z(t)\big).
\end{aligned} \tag{A.11}$$

Consider the representation of the radiator flow rates using the scaling factor ξ_r of the zonal average flow rate as

$$q_{\mathrm{rad},r} = \xi_r \frac{q_{\mathrm{zon},z}}{Q_z}, \tag{A.12}$$

With such a representation, equal flow rate in all radiators, $q_{\mathrm{rad},P_z} = \ldots = q_{\mathrm{rad},R_z}$ correspond to a scaling factor of $\xi_r = 1$ for all radiators $r = P_z, \ldots, R_z$. Using Eq. (A.12), the error in Eq. (A.11) can be written as

$$\begin{aligned}
&\tilde{\Phi}_{\mathrm{zon},z} - \sum_{r=P_z}^{R_z} \Phi_r \\
&= c_p \left(\sum_{n=1}^{\infty} \frac{K_z^n}{n!} \left(\frac{Q_z^n}{q_{\mathrm{zon},z}^{n-1}} - \sum_{r=P_z}^{R_z} \frac{Q_z^{n-1}}{\xi^{n-1}\, q_{\mathrm{zon},z}^{n-1}} \right) \right) \big(u(t) - y_z(t)\big) \\
&= c_p \left(\sum_{n=1}^{\infty} \frac{K_z^n\, Q_z^{n-1}}{n!\, q_{\mathrm{zon},z}^{n-1}} \left(Q_z - \sum_{r=P_z}^{R_z} \frac{1}{\xi^{n-1}} \right) \right) \big(u(t) - y_z(t)\big),
\end{aligned} \tag{A.13}$$

From Eq. (A.13), each term in the Taylor expansion is separated into multiple factors: the approximation error will increase with K_z and decrease with the zonal average flow rate $q_{\mathrm{zon},z}/Q_z$, and it also depends on flow rate distribution between the zone's radiators' scaling factors $\xi_{P_z}, \ldots, \xi_{R_z}$. When all radiator flow rates $q_{\mathrm{rad},r}$ are equal, i.e., $\xi_{P_z} = \ldots = \xi_{R_z} = 1$, the single radiator formulation of Eq. (A.10) is equivalent to the summed radiator heating power given Eq. (A.8), i.e., $\tilde{\Phi}_{\mathrm{zon},z} = \sum_{r=P_z}^{R_z} \Phi_r$.

Appendix B. Bounds on post-rebalanced heat supply coefficients

The derivative of Eq. (10) is

$$\begin{aligned}
\nu_z'(q_{\mathrm{zon},z}) &= \underbrace{C_z\, c_p}_{\geq 0} \left(1 - \underbrace{\left(1 + \frac{Q_z\, L_z\, m_z}{c_p\, q_{\mathrm{zon},z}} \right) \exp\left(-\frac{Q_z\, L_z\, m_z}{c_p\, q_{\mathrm{zon},z}} \right)}_{\leq 1} \right) \\
&\geq 0
\end{aligned} \tag{B.1}$$

i.e., the heat supply coefficient ν_z is monotonically increasing in the zonal flow rate $q_{\mathrm{zon},z}$. Given the identified value of the heat supply coefficient $\nu_z(\tilde{q}_{\mathrm{zon},z})$, we use the property of monotonically increasing of $\nu_z(q_{\mathrm{zon},z})$, as shown by Eq. (B.1), to establish the bound

$$\begin{cases} \nu_z(\tilde{q}_{\mathrm{zon},z} + \Delta q_{\mathrm{zon},z}) \leq \nu_z(\tilde{q}_{\mathrm{zon},z}) & \text{if } \Delta q_{\mathrm{zon},z} \in \left[-\tilde{q}_{\mathrm{zon},z}, 0 \right] \\ \nu_z(\tilde{q}_{\mathrm{zon},z}) \leq \nu_z(\tilde{q}_{\mathrm{zon},z} + \Delta q_{\mathrm{zon},z}) & \text{if } \Delta q_{\mathrm{zon},z} \in [0, \infty]. \end{cases} \tag{B.2}$$

Further, the second derivative of Eq. (10) is

$$\nu_z''(q_{\mathrm{zon},z}) = -C_z\, c_p\, \frac{L_z^2\, m_z^2\, Q_z^2}{c_p^2\, q_{\mathrm{zon},z}^3} \exp\left(-\frac{Q_z\, L_z\, m_z}{c_p\, q_{\mathrm{zon},z}} \right) \leq 0, \tag{B.3}$$

i.e., since $0 \leq C_z$, $\nu_z(q_{\mathrm{zon},z})$ is concave. Besides the known value of $\nu_z(\tilde{q}_{\mathrm{zon},z})$, Eq. (10) gives $\nu_z(0) = 0$ for any values of the coefficient C_z, L_z, and m_z. Writing the secant between $q_{\mathrm{zon},z} = 0$ and $q_{\mathrm{zon},z} = \tilde{q}_{\mathrm{zon},z}$ as

$$s(\tilde{q}_{\mathrm{zon},z} + \Delta q_{\mathrm{zon},z}) = \nu_z(\tilde{q}_{\mathrm{zon},z}) + \Delta q_{\mathrm{zon},z} \frac{\nu_z(\tilde{q}_{\mathrm{zon},z})}{\tilde{q}_{\mathrm{zon},z}}, \tag{B.4}$$

the concavity of $\nu_z(q_{\mathrm{zon},z})$ gives

$$\begin{cases} s(\tilde{q}_{\mathrm{zon},z} + \Delta q_{\mathrm{zon},z}) \leq \nu_z(\tilde{q}_{\mathrm{zon},z} + \Delta q_{\mathrm{zon},z}) \\ \qquad\qquad \text{if } \Delta q_{\mathrm{zon},z} \in \left[-\tilde{q}_{\mathrm{zon},z}, 0 \right] \\ \nu_z(\tilde{q}_{\mathrm{zon},z} + \Delta q_{\mathrm{zon},z}) \leq s(\tilde{q}_{\mathrm{zon},z} + \Delta q_{\mathrm{zon},z}) \\ \qquad\qquad \text{if } \Delta q_{\mathrm{zon},z} \in [0, \infty) \end{cases} \tag{B.5}$$

Thus, by combining Eqs. (B.2) and (B.5), we obtain the lower and upper bounds in Eq. (25).

References

[1] European Commission — Department: Energy, In Focus: Energy Efficiency in Buildings - European Commission, 2020, https://commission.europa.eu/news/focus-energy-efficiency-buildings-2020-02-17_en.

[2] European parliament, council of the European union, Directive (EU) 2024/1275 of the European parliament and of the council of 24 april 2024 on the energy performance of buildings, Off. J. Eur. Union (2024). https://eur-lex.europa.eu/eli/dir/2024/1275/oj.

[3] E.H. Industry, Heating Market Report 2023, Technical Report, European Heating Industry, 2023. https://ehi.eu/wp-content/uploads/2024/04/2023_EHI_ANNUALREPORT.pdf.

[4] P. Johansson, Heat pumps in Sweden – a historical review, Energy 229 (2021) 120683. https://doi.org/10.1016/j.energy.2021.120683

[5] S. Werner, International review of district heating and cooling, Energy 137 (2017) 617–631. https://doi.org/10.1016/j.energy.2017.04.045

[6] D. Teli, T. Psomas, S. Langer, A. Trüschel, J.-O. Dalenbäck, Drivers of winter indoor temperatures in Swedish dwellings: investigating the tails of the distribution, Build. Environ. 202 (2021) 108018. https://doi.org/10.1016/j.buildenv.2021.108018

[7] D. Olsson, P. Filipsson, A. Trüschel, Feedback control in Swedish multi-family buildings for lower energy demand and assured indoor temperature–measurements and interviews, Energies 16 (18) (2023) 6747. Number: 18 Publisher: Multidisciplinary Digital Publishing Institute, https://doi.org/10.3390/en16186747

[8] R. American Society of Heating, I.A. Air-Conditioning Engineers, 2020 ASHRAE Handbook - Heating, Ventilating, and Air-Conditioning Systems and Equipment, American Society of Heating, Refrigerating and Air-Conditioning Engineers, Inc. (ASHRAE), 2020. Publication Title: 2020 ASHRAE Handbook - HVAC Systems and Equipment (SI Edition), https://app.knovel.com/hotlink/toc/id:kpASHRAEY7/ashrae-handbook-hvac/ashrae-handbook-hvac.

[9] S. Prívara, J. Široký, L. Ferkl, J. Cigler, Model predictive control of a building heating system: the first experience, Energy Build. 43 (2) (2011) 564–572. https://doi.org/10.1016/j.enbuild.2010.10.022

[10] T. Cholewa, I. Balen, A. Siuta-Olcha, On the influence of local and zonal hydraulic balancing of heating system on energy savings in existing buildings – long term experimental research, Energy Build. 179 (2018) 156–164. https://doi.org/10.1016/j.enbuild.2018.09.009

[11] F. Tahersima, J. Stoustrup, H. Rasmussen, An analytical solution for stability-performance dilemma of hydronic radiators, Energy Build. 64 (2013) 439–446. https://doi.org/10.1016/j.enbuild.2013.05.023

[12] D.S. Østergaard, S. Svendsen, Experience from a practical test of low-temperature district heating for space heating in five Danish single-family houses from the 1930s, Energy 159 (2018) 569–578. https://doi.org/10.1016/j.energy.2018.06.142

[13] A. Trüschel, Hydronic Heating Systems the Effect of Design on System Sensitivity, number 1857 in Doktorsavhandlingar vid Chalmers tekniska högskola, Chalmers Univeristy of Technology, 2002. https://research.chalmers.se/en/publication/526.

[14] E.A. Piana, B. Grassi, F. Bianchi, C. Pedrotti, Hydraulic balancing strategies: a case study of radiator-based central heating system, Build. Serv. Eng. Res. Technol. 39 (3) (2018) 249–262. Publisher: SAGE Publications Ltd STM, https://doi.org/10.1177/0143624417752830

[15] D.S. Østergaard, M. Tunzi, S. Svendsen, What does a well-functioning heating system look like? investigation of ten Danish buildings that utilize district heating efficiently, Energy 227 (2021) 120250. https://doi.org/10.1016/j.energy.2021.120250

[16] A. Trüschel, The Value of Balancing, Technical Report 2005:134, Svensk fjärrvärme, G, 2005. https://citrenergy.se/knowledgebank/vardet-av-injustering/.

[17] S. Månsson, P.-O. Johansson Kallioniemi, M. Thern, T. Van Oevelen, K. Sernhed, Faults in district heating customer installations and ways to approach them: experiences from Swedish utilities, Energy 180 (2019) 163–174. https://doi.org/10.1016/j.energy.2019.04.220

[18] L. Zhang, J. Xia, J.E. Thorsen, O. Gudmundsson, H. Li, S. Svendsen, Method for achieving hydraulic balance in typical Chinese building heating systems by managing differential pressure and flow, Build. Simul. 10 (1) (2017) 51–63. https://doi.org/10.1007/s12273-016-0307-2

[19] F. Pedranzini, L.P.M. Colombo, F. Romano, Development and application of a novel non-iterative balancing method for hydronic systems, Appl. Sci. 14 (14) (2024) 6232. Number: 14 Publisher: Multidisciplinary Digital Publishing Institute, https://doi.org/10.3390/app14146232

[20] H. Averfalk, S. Werner, Essential improvements in future district heating systems, Energy Procedia 116 (2017) 217–225. https://doi.org/10.1016/j.egypro.2017.05.069

[21] C. Naldi, M. Dongellini, G.L. Morini, E. Rossi di Schio, The adoption of pressure independent control valves (PICVs) for the simultaneous optimization of energy consumption and comfort in buildings, Energy Build. 287 (2023) 112969. https://doi.org/10.1016/j.enbuild.2023.112969

[22] M. Tunzi, D. Skaarup Østergaard, S. Svendsen, Development and test of a novel electronic radiator thermostat with a return temperature limiting function, Energies 15 (1) (2022) 367. Number: 1 Publisher: Multidisciplinary Digital Publishing Institute, https://doi.org/10.3390/en15010367

[23] V. Edenhofer, D. Olsson, Elektroniska Termostater I Flerbostadshus, Prestudy 2023:08, Bebostad, 2024. https://www.bebostad.se/projekt/avslutade-projekt/2022/2022-behovsanpassad-varmereglering-forstudie.

[24] H.-I. Cho, D. Cabrera, M.K. Patel, Estimation of energy savings potential through hydraulic balancing of heating systems in buildings, J. Build. Eng. 28 (2020) 101030. https://doi.org/10.1016/j.jobe.2019.101030

[25] L. Sarran, K.M. Smith, C.A. Hviid, C. Rode, Grey-box modelling and virtual sensors enabling continuous commissioning of hydronic floor heating, Energy 261 (2022) 125282. https://doi.org/10.1016/j.energy.2022.125282

[26] Z. Afroz, G.M. Shafiullah, T. Urmee, G. Higgins, Modeling techniques used in building HVAC control systems: a review, Renewable Sustainable Energy Rev. 83 (2018) 64–84. https://doi.org/10.1016/j.rser.2017.10.044

[27] J. Drgoňa, J. Arroyo, I. Cupeiro Figueroa, D. Blum, K. Arendt, D. Kim, E.P. Ollé, J. Oravec, M. Wetter, D.L. Vrabie, L. Helsen, All you need to know about model predictive control for buildings, Annu. Rev. Contr. 50 (2020) 190–232. https://doi.org/10.1016/j.arcontrol.2020.09.001

[28] P. Bacher, H. Madsen, Identifying suitable models for the heat dynamics of buildings, Energy Build. 43 (7) (2011) 1511–1522. https://doi.org/10.1016/j.enbuild.2011.02.005

[29] L.H. Hansen, Stochastic Modelling of Central Heating Systems, IMM-PHD-1997-34, Technical University of Denmark, Kgs. Lyngby, 1997.

[30] C.A. Thilker, P. Bacher, H.G. Bergsteinsson, R.G. Junker, D. Cali, H. Madsen, Nonlinear grey-box modelling for heat dynamics of buildings, Energy Build. 252 (2021) 111457. https://doi.org/10.1016/j.enbuild.2021.111457

[31] M. Eide Bagle, P. Maree, H. Taxt Walnum, I. Sartori, Identifying grey-box models from archetypes of apartment block buildings, in: Proceedings of Building Simulation 2021, 17 of *Building Simulation*, IBPSA, Bruges, Belgium, 2021, pp. 1091–1098. https://doi.org/10.26868/25222708.2021.30162

[32] T.H. Pedersen, R.E. Hedegaard, K.F. Kristensen, B. Gadgaard, S. Petersen, The effect of including hydronic radiator dynamics in model predictive control of space heating, Energy Build. 183 (2019) 772–784. https://doi.org/10.1016/j.enbuild.2018.11.015

[33] W.J. Rugh, Linear System Theory, Prentice Hall Information and System Sciences Series, Prentice Hall, Upper Saddle River, N.J, 2nd ed edition, 1996.

[34] L. Olsson Ingvarson, S. Werner, Building mass used as short term heat storage, in: 11th International Symposium on District Heating and Cooling, Reykjavik, Iceland, August 31–September 2, 2008, 2008.